Stress-based topological shape optimization for thick shells using the level set method and trimmed non-conforming multi-patch isogeometric analysis

Fernando Hübner Scherer, Malek Zarroug, Hakim Naceur, Andrei Constantinescu

Stress-based topological shape optimization for thick shells using the level set method and trimmed non-conforming multi-patch isogeometric analysis

Fernando Hübner[1,2,3*], Malek Zarroug[2], Hakim Naceur[3], Andrei Constantinescu[1]

[1*]Laboratoire de Mécanique des Solides, CNRS, École Polytechnique, Route de Saclay, Palaiseau, 91128, France.
[2]Groupe Stellantis, Route de Gisy, Velizy-Villacoublay, 78140, France.
[3]INSA Hauts de France, CNRS, UMR 8201 - LAMIH, F-59313, Valenciennes, France.

Contributing authors: andrei.constantinescu@polytechnique.edu;

Abstract

This paper introduces a novel method for optimal shape design of thick shells. We consider shells based on the Reissner-Mindlin theory, with the assumption of linear elastic material behavior. The goal is to find the optimal material distribution within the shell's mid-surface. This is achieved using a cost function that minimizes the volume while considering stress-based constraints, with the material distribution represented by a level set function. The evolution of the shape is driven by the gradient of the cost function within the framework of a Hamilton-Jacobi equation. Both the level set and the displacement fields are described using computer aided design compatible tools, within the framework of isogeometric analysis. This allows for precise definition of the optimal shape and straightforward export of the resulting design to commercial software for manufacturing. Furthermore, the proposed method handles complex, non-conforming multi-patch geometries thanks to an augmented Lagrangian formulation. The latter guarantees strong compatibility with real-world engineering applications. The effectiveness of the method is demonstrated through its application to various three-dimensional multi-patch geometries under different loading conditions.

Keywords: Topology optimization, Isogeometric analysis, Level set method, Reissner-Mindlin shells, non-conforming multi-patch

Published in SAMO, 2024. DOI: https://doi.org/10.1007/s00158-024-03892-x

1 Introduction

Stress-based optimization stands as a cornerstone in engineering practices, as it preemptively allows to address critical issues such as stress concentration, crack propagation, structural failure, and fatigue. An effective and robust technique to address topology optimization (TO) problems is the level set method, as demonstrated in Allaire and Jouve (2008); Allaire et al. (2004); Allaire and Jouve (2005); Amstutz and Andrä (2006); Amstutz and Novotny (2010); Picelli et al. (2018), which has been extensively coupled with the finite element method (FEM) for the numerical analysis. These works have seeded instrumental tool for engineering practices such as microstructure design and additive manufacturing, as presented in Agnelli et al. (2022); Nika and Constantinescu (2019); Agnelli et al. (2020); Alacoque et al. (2021).

However, since numerous industrial engineering applications are based on computer-aided design (CAD) geometries, topological optimization algorithms based on FEM have the drawback of producing an output that requires pre- and post-processing operations to reconstruct a useful CAD geometry. To overcome this problem in density-based TO methods, such as the Solid Isotropic Material with Penalization (SIMP), the density field can be modeled as a NURBS surface, which has been demonstrated to be effective in a range of applications, from stiffness maximization with anisotropy T. Roiné and Pailhès (2022) to stress-related problems Montemurro et al. (2024); Montemurro and Roiné (2024). Another possibility to overcome this problem is to use isogeometric analysis (IGA) T.J.R. Hughes (2009), which provides in-loop CAD compatibility. For instance, Gao et al. (2022) proposed a TO method to minimize the level set method (LSM) compliance on composite structure for single-piece 2D and 3D volumetric isogeometric elements. Seo et al. (2010a,b); Kang and Youn (2016) implemented nucleation techniques on trimmed surfaces to extend parametric optimization to incorporate topology changes on single-patch isogeometric shell elements. Furthermore, stress-based optimization using IGA has also been shown to work with the LSM Jahangiry et al. (2022) and density-based approaches such as the SIMP method Liu et al. (2018). Nevertheless, we believe that further improvements to stress-based TO on shell isogeometric elements in nonconforming multi-patch isogeometric analysis are still needed.

In Hübner Scherer et al. (2024), we presented a TO method for compliance minimization that combines the level set method and non-conforming multi-patch IGA. In the present paper, we extend this approach to stress-based optimization, with particular interest on the minimization of the L^p norm of the von Mises stress. In this study, we derive an alternative formulation for the shape derivative, given by a tensor representation. We also extend the method to solve multi-patch problems with an augmented Lagrangian approach based on Adam et al. (2020) which increases the algorithmic robustness of multi-patch problems.

This work is structured as follows: Section 2 introduces the Reissner-Mindlin shell model for isogeometric analysis. Section 3 introduces the level set method for non-conforming NURBS surfaces. Section 5 combines the isogeometric and level set approaches in an augmented Lagrangian setting. The optimization setting and the expression of the shape derivative are presented in Section 6. Finally, the numerical results are elaborated in Section 7, and conclusions are drawn in Section 8.

2 Reissner-Mindlin shells with IGA

The problem of the linear elastic thick shell under the Reissner-Mindlin kinematic assumption is introduced using isogeometric analysis, as previously developed in Hübner Scherer et al. (2024). The domain of optimization, denoted by $\mathcal{D}$, will be introduced initially as a single-patch NURBS surface corresponding to the mid-surface of the shell and will later be generalized to a non-conforming multi-patch domain. For further insight into the development of an IGA solver for linear elastic Reissner-Mindlin shells, refer to Benson et al. (2010); Adam (2020), and for fundamental principles of shell modeling and differential geometry, see Ciarlet and Mardare (2008).

Notation. In the present paper, we employ the Einstein summation convention over repeated indices, where Greek indices and exponents $\alpha, \beta, \mu, \lambda$ have values in $\{1, 2\}$, while Latin lowercase indices i, j, r, s range in $\{1, 2, 3\}$. Furthermore, the symbol $(\hat{\ })$ is used to emphasize the parametric nature of a mathematical entity.

Let us introduce the NURBS parameterization $\mathbf{S}$ of the mid-surface, constructed as a two-dimensional tensor product structure that is fully determined by the knot vectors Ξ_α, the degrees d_α and the net of $n_1 \cdot n_2$ control points $\{\mathbf{X}_B\}_{B=1}^{n_1 \cdot n_2}$:

$$\mathbf{S} : \hat{\mathcal{D}} \subset \mathbb{R}^2 \to \mathbb{R}^3 \qquad \mathbf{S}(\xi_1, \xi_2) = \sum_{B=1}^{n_1 \cdot n_2} R_B(\xi_1, \xi_2) \mathbf{X}_B \tag{1}$$

where $\{R_B\}_{B=1}^{n_1 \cdot n_2}$ denotes the rational B-splines basis functions, $\hat{\mathcal{D}}$ is the parametric domain and the integers n_α are related to the size of the knot vector by the relation $n_\alpha = \mathrm{Card}(\Xi_\alpha) - d_\alpha - 1$.

This parameterization naturally defines the mid-surface $\mathcal{D}$ of the shell with $\mathcal{D} = \mathbf{S}(\hat{\mathcal{D}})$. In each point of this surface, we define the in-plane covariant basis $\{\mathbf{a}_i\}$ by the derivatives with respect to the parametric domain: $\mathbf{a}_\alpha = \hat{\partial}_\alpha \mathbf{S}$ and $\mathbf{a}_3 = \frac{\hat{\partial}_1 \mathbf{S} \times \hat{\partial}_2 \mathbf{S}}{|\hat{\partial}_1 \mathbf{S} \times \hat{\partial}_2 \mathbf{S}|}$. The covariant vectors $\{\mathbf{g}_i\}$ extend this concept to the whole volume of the shell and are computed with $\mathbf{g}_\alpha = \hat{\partial}_\alpha \boldsymbol{\mathcal{V}} = \mathbf{a}_\alpha + \xi_3 \hat{\partial}_\alpha \mathbf{a}_3$ and $\mathbf{g}_3 = \hat{\partial}_3 \boldsymbol{\mathcal{V}} = \mathbf{a}_3$. Additionally, both of these vectors define in a similar fashion their contravariant counterparts by $\mathbf{g}^j \cdot \mathbf{g}_i = \delta_i^j$ and $\mathbf{a}^j \cdot \mathbf{a}_i = \delta_i^j$, where δ_i^j is the Kronecker symbol. Finally, the covariant and contravariant components of the metric tensor are given by $g_{ij} = \mathbf{g}_i \cdot \mathbf{g}_j$ and $g^{ij} = \mathbf{g}^i \cdot \mathbf{g}^j$, respectively.

The covariant basis allows us to define the thick shell of constant thickness $\epsilon > 0$ as the image of the *parametric volume map* $\boldsymbol{\mathcal{V}}$ given by:

$$\boldsymbol{\mathcal{V}} : \hat{\mathcal{D}} \times \left[-\frac{\epsilon}{2}, \frac{\epsilon}{2}\right] \to \mathbb{R}^3 \qquad \boldsymbol{\mathcal{V}}((\xi_1, \xi_2), \xi_3) = \mathbf{S}(\xi_1, \xi_2) + \xi_3 \mathbf{a}_3(\xi_1, \xi_2). \tag{2}$$

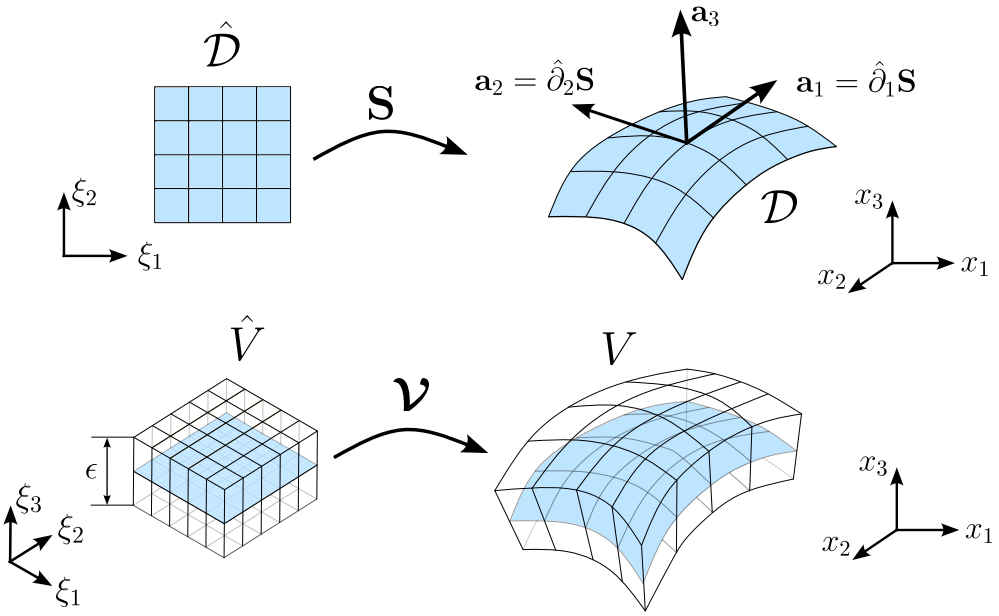

Fig. 1: The construction of the thick shell: (top panel) The *mid-surface function* $\mathbf{S} : \hat{\mathcal{D}} \to \mathcal{D}$ maps a point of the parametric domain $\hat{\mathcal{D}}$ into a point in the physical domain, namely the mid-surface $\mathcal{D}$. (bottom panel) The *parametric volume function* $\boldsymbol{\mathcal{V}} : \hat{V} \to V$ maps a point of the parametric volume $\hat{V} = \hat{\mathcal{D}} \times \left[-\frac{\epsilon}{2}, \frac{\epsilon}{2}\right]$ into a point in the physical volume V.

2.1 Mechanics

Let us now take into consideration the kinematic assumption of the Reissner-Mindlin shell model. The displacement field $\mathbf{u}^V$ in the volume is assumed to be decomposed into the displacement $\mathbf{u}^{\mathcal{D}} : \hat{\mathcal{D}} \to \mathbb{R}^3$ of the mid-surface and a rotation $\mathbf{r} : \hat{\mathcal{D}} \to \mathbb{R}^3$ along its normal:

$$\mathbf{u}^V(\xi_1, \xi_2, \xi_3) = \mathbf{u}^{\mathcal{D}}(\xi_1, \xi_2) + \xi_3 \mathbf{r}(\xi_1, \xi_2) \times \mathbf{a}_3(\xi_1, \xi_2). \tag{3}$$

The covariant components of the small strain tensor are written in terms of the geometry of the shell as:

$$\varepsilon_{ij}(\mathbf{u}^V) = \frac{1}{2}\left(\mathbf{g}_i \cdot \hat{\partial}_j \mathbf{u}^V + \mathbf{g}_j \cdot \hat{\partial}_i \mathbf{u}^V\right). \tag{4}$$

Let us consider a homogeneous material under the assumption of isotropic and linear elastic behavior, with a constitutive tensor A^{ijrs} defined from the Young's modulus E and the Poisson's ratio ν. Then, the stresses can be calculated with the generalized Hooke's law under the small strains assumption:

$$\sigma^{ij} = A^{ijrs}\varepsilon_{rs}, \tag{5}$$

This constitutive relation can be further refined in terms of the contravariant components of the metric tensor of the shell Adam et al. (2020), by separating membrane/bending and shearing stresses:

$$\begin{cases} \sigma^{\alpha\beta} = H^{\alpha\beta\lambda\mu}\varepsilon_{\lambda\mu}, & H^{\alpha\beta\lambda\mu} = \dfrac{E}{2(1+\nu)}\left(g^{\alpha\lambda}g^{\beta\mu} + g^{\alpha\mu}g^{\beta\lambda} + \dfrac{2\nu}{1-\nu}g^{\alpha\beta}g^{\lambda\mu}\right) \\ \sigma^{\alpha 3} = \dfrac{1}{2}G^{\alpha\lambda}\varepsilon_{\lambda 3}, & G^{\alpha\lambda} = \dfrac{2E}{1+\nu}g^{\alpha\lambda}. \end{cases} \tag{6}$$

Consequently, the virtual internal work of the stress associated with a displacement $\mathbf{u}$ can be transformed by this constitutive relation into the following expression for a virtual displacement field $\mathbf{v}$:

$$\int_V \sigma(\mathbf{u}) : \varepsilon(\mathbf{v})\,\mathrm{d}V = \int_V H^{\alpha\beta\lambda\mu}\varepsilon_{\lambda\mu}(\mathbf{u})\varepsilon_{\alpha\beta}(\mathbf{v}) + G^{\alpha\beta}\varepsilon_{\alpha 3}(\mathbf{u})\varepsilon_{\beta 3}(\mathbf{v})\,\mathrm{d}V \tag{7}$$

In addition, the shell is subjected to external loads in the region labeled $\partial\mathcal{D}_N$ and assumed to be fixed along the portion $\partial\mathcal{D}_D$. The remaining portion of the boundary constitutes a traction-free region labeled $\partial\mathcal{D}_0$. Consequently, the complete boundary $\partial\mathcal{D}$ is partitioned into subsets as $\partial\mathcal{D} = \partial\mathcal{D}_D \cup \partial\mathcal{D}_N \cup \partial\mathcal{D}_0$.

As a consequence of the kinematic assumption of the Reissner-Mindlin shell, we also decompose the Dirichlet boundary $\partial\mathcal{D}_D$ into a portion $\partial\mathcal{D}_D^U$, where zero displacement is imposed, and $\partial\mathcal{D}_D^R$, wherein no rotation is permitted. This decomposition induces the following functional space of the admissible displacement functions:

$$H_D^1(\mathcal{D}) = \{\mathbf{v} = (\mathbf{v}^U, \mathbf{v}^R) \in H^1(\mathcal{D}) \times H^1(\mathcal{D}) : \quad \mathbf{v}^U|_{\partial\mathcal{D}_D^U} = \mathbf{0}, \quad \mathbf{v}^R|_{\partial\mathcal{D}_D^R} = \mathbf{0}\}, \tag{8}$$

The elastic Reissner-Mindlin thick-shell can then be formulated with the following variational problem:

Find the displacement field $\mathbf{u} \in H_D^1(\mathcal{D})$ such that:

$$\int_V \sigma(\mathbf{u}) : \varepsilon(\mathbf{v})\,\mathrm{d}V = \int_V \mathbf{f}^V \cdot \mathbf{v}\,\mathrm{d}V + \int_{\mathcal{D}} \mathbf{f}^S \cdot \mathbf{v}\,\mathrm{d}\mathcal{D} + \int_{\partial\mathcal{D}_N} \left(\mathbf{v}^U \cdot \mathbf{g} + \mathbf{v}^R \cdot \mathbf{m}\right) ds \tag{9}$$

for any test function $\mathbf{v} \in H_D^1(\mathcal{D})$.

In this variational problem, we denote $\mathbf{f}^S$ as the surface tension applied solely on the mid-section $\mathcal{D}$, $\mathbf{f}^V$ as the volumetric force, $\mathbf{m}$ as the moment applied to $\partial\mathcal{D}_N$, and $\mathbf{g}$ as the lateral traction applied to $\partial\mathcal{D}_N$.

It is widely acknowledged that thick shells can be susceptible to numerical locking and yield less reliable results when standard finite elements do not account for shear deformation and thickness effects. To mitigate locking issues, a reduced integration technique is employed, which is particularly effective for NURBS approximations with degrees greater than two. Although the current investigation does not treate the shape optimization through the thickness, we assert that our method remains applicable to

thin-shell models. Moreover, we advocate for the use of thick-shell models as it offers a robust framework capable of accommodating future enhancements, in particular the optimization of the thickness profile of the shell.

2.2 Extension to multi-patch isogeometric analysis

Let us consider extending the previous definitions to geometries composed of sereval individual patches. For such purposes, we introduce a collection $\{\mathbf{S}_k\}_{k=1}^K$ of K non-overlapping NURBS parameterizations. Each map $\mathbf{S}_k$ defines a mid-surface $\mathcal{D}_k$ obtained from $\mathcal{D}_k = \mathbf{S}_k(\hat{\mathcal{D}}_k)$. The collection $\{\mathcal{D}_k\}_{k=1}^K$ forms a partition of the mid-surface $\mathcal{D}$ with:

$$\overline{\mathcal{D}} = \bigcup_{k=1}^{K} \overline{\mathcal{D}}_k \quad \text{where} \quad \mathcal{D}_k \cap \mathcal{D}_l = \emptyset \quad \text{if} \quad k \neq l. \tag{10}$$

The interface γ_{kl} between two patches is given by:

$$\gamma_{kl} = \overline{\partial\mathcal{D}_k \cap \partial\mathcal{D}_l} \quad \text{with} \quad 1 \leq k < l \leq K. \tag{11}$$

3 Level set representation of the material domain

We briefly introduce the setting proposed in Hübner Scherer et al. (2024) to define a multi-patch shape $\Omega \subset \mathcal{D}$ using the level set technique. For a given patch k, we denote with $\mathbf{S}_k$ its parameterization, which yields a mid-surface $\mathcal{D}_k = \mathbf{S}_k(\hat{\mathcal{D}}_k)$. By introducing a level set function $\phi_k : \mathcal{D}_k \to \mathbb{R}$, the *material phase* is defined as a subset of the mid-surface $\mathcal{D}_k$ with:

$$\Omega_k = \{\boldsymbol{x} \in \mathcal{D}_k : \phi_k(\boldsymbol{x}) < 0\} \tag{12}$$

The parametric construction of the mid-surface $\mathcal{D}_k$ naturally defines the *pullback operator* of ϕ_k by $\mathbf{S}_k$ as the function $\hat{\phi}_k : \hat{\mathcal{D}}_k \to \mathbb{R}$ given by the following expression:

$$\hat{\phi}_k(\boldsymbol{\xi}) = \phi_k(\mathbf{S}_k(\boldsymbol{\xi})) \qquad \forall \boldsymbol{\xi} \in \hat{\mathcal{D}}_k \tag{13}$$

The *parametric material phase* $\hat{\Omega}_k$ is the parametric counterpart of the shape Ω_k. It is defined by means of the pullback operator:

$$\hat{\Omega}_k = \{\boldsymbol{\xi} \in \hat{\mathcal{D}}_k : \hat{\phi}_k(\boldsymbol{\xi}) < 0\} = \mathbf{S}_k^{-1}(\Omega_k) \tag{14}$$

Given that the map $\mathbf{S}_k$ is a diffeomorphism from $\hat{\mathcal{D}}_k$ onto $\mathcal{D}_k$, it is straightforward to verify that:

$$\phi_k(\boldsymbol{x}) = \hat{\phi}_k(\mathbf{S}_k^{-1}(\boldsymbol{x})) \qquad \forall \boldsymbol{x} \in \mathcal{D}_k \tag{15}$$

When we consider a collection of level set functions $\phi = \{\phi_k\}_{k=1}^K$, a sequence of shapes $\{\Omega_k\}_{k=1}^K$ is directly obtained from equation (12). The global multi-patch shape Ω is then defined as the union of the single-patch shapes Ω_k:

$$\overline{\Omega} = \bigcup_{k=1}^{K} \overline{\Omega}_k \tag{16}$$

The level set technique consists of subdividing the domain into two regions with distinct material behavior, as depicted in Figure 2. The *material phase* Ω_k (or *strong phase*) has the strong material properties of the component that is being optimized, whereas the *weak phase* $\mathcal{D}_k \setminus \Omega_k$ (also called *void phase* or *ersatz material*) has weaker material properties, so that it behaves as a void region.

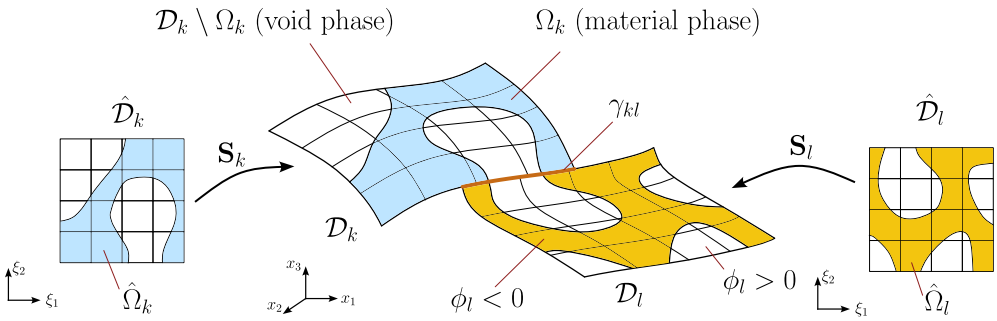

Fig. 2: Illustration on the coupling of the level set method with non-conforming multi-patch NURBS surfaces. For the patch k, the material phases Ω_k in blue is defined as the set of points in the mid-surface $\mathcal{D}_k$ where the level set function ϕ_k is negative. The set $\mathcal{D}_k \setminus \Omega_k$ is named the *void phase* which acts as a void region, because of its weak material properties. The parametric material phase $\hat{\Omega}_k$ is defined in a similar fashion as the set of points in the parametric domain $\hat{\mathcal{D}}_k$ where $\hat{\phi}_k$ is negative.

Let us now model the evolution of the shape Ω_k in the course of a pseudo-time $t > 0$. We track the evolution of a material point, initially at position $\boldsymbol{x} \in \mathcal{D}$, which is assumed to be moving with a given velocity field $\boldsymbol{v}_k(\boldsymbol{x}, t)$. This velocity field is assumed for now to be a descent direction of a certain cost functional $\mathcal{J}$, which will later be established in Section 6. For an arbitrary boundary point $\boldsymbol{x}(t) \in \partial\Omega_k(t)$, it holds that $\phi_k(\boldsymbol{x}(t), t) = 0$. By differentiating this equation with respect to the pseudo-time t, one obtains the equation that governs the evolution of the shape Ω_k, known as the Hamilton-Jacobi equation. In multi-patch non-conforming isogeometric analysis, we consider writing this equation, along with its boundary conditions, as:

$$\begin{cases} \dfrac{\partial \phi_k}{\partial t} + \boldsymbol{v}_k \cdot \nabla_{\mathcal{D}} \phi_k = 0 & \text{in } \mathcal{D}_k \times (0, \infty) \\ \phi_k(\cdot, 0) = \phi_k^0 & \text{in } \mathcal{D}_k \\ \nabla_{\mathcal{D}} \phi_k \cdot \mathbf{t}_N = 0 & \text{on } \partial\mathcal{D}_k \setminus \cup_{l=1, l\neq k}^{K} \gamma_{kl} \\ \mathrm{tr}_{kl} \phi_k - \mathrm{tr}_{lk} \phi_l = 0 & \text{on } \cup_{l=1, l\neq k}^{K} \gamma_{kl} \end{cases} \tag{17}$$

where $\mathbf{t}_N \in T(\mathcal{D}_k)$ is the unit outward normal to $\partial\mathcal{D}_k$ in the tangent space and $(\nabla_{\mathcal{D}} \phi_k)_\alpha = \frac{\partial \phi_k}{\partial l_\alpha} \frac{\mathbf{a}_\alpha}{|\mathbf{a}_\alpha|}$ is the gradient operator written in the local coordinates system in the physical domain and ϕ_k^0 is a known initialization function of the level set at the patch k.

In numerical practice, the graph of the pullback operator $\hat{\phi}_k$ of the level set function is modeled as a NURBS surface. This allows for accurate numerical integration as a consequence of the precise delination of the boundaries of the parametric material phase $\hat{\Omega}_k$. In addition, by computing the intersection of $\hat{\phi}_k$ with the plane $\xi_3 = 0$, one obtains a set of closed parametric curves, which permits the visualization of a trimmed surface Marussig and Hughes (2018). These p-curves are also mapped into the physical domain by $\mathbf{S}_k$, which yield the boundaries of Ω_k as a set of B-spline curves.

To numerically solve equation (17), we applied the computational method previously introduced in Hübner Scherer et al. (2024) for non-conforming patches. In this approach, we introduced a discrete counterpart $[\phi_k]$ of the level set function evaluated on a uniform discretetization $[\hat{G}_k]$ of the parametric grid. We employed $[\phi_k]$ to solve the equation is independently for each patch using an upwind finite difference scheme, based on the Lax-Friedrichs flux Osher and Shu (1991); Laurain (2018). At the patch boundaries, the scheme is adapted to incorporate information regarding the level set function of neighboring patches.

4 Trimming surfaces with level set functions

The aim of this section is to establish a methodology for conducting numerical integration on a multi-patch domain $\mathcal{D}$, which is trimmed by a level set function $\phi_k : \mathcal{D}_k \to \mathbb{R}$. We begin by recalling the standard procedure in isogeometric analysis for computing integrals over curved domains. The parameter space is divided into a set of elements, each defined as the Cartesian product of the span between two consecutive points in the knot vector of each parametric direction. Figure 3 illustrates how an element, denoted by $\hat{\mathcal{D}}_k^e$, is mapped from the parametric space into an element $\mathcal{D}_k^e$ of the physical space. Finally, numerical integration can be performed using NURBS-enhaced Gaussian integration, as described in Sevilla et al. (2008a,b), by mapping each element $\hat{\mathcal{D}}_k^e$ into the unit square reference element.

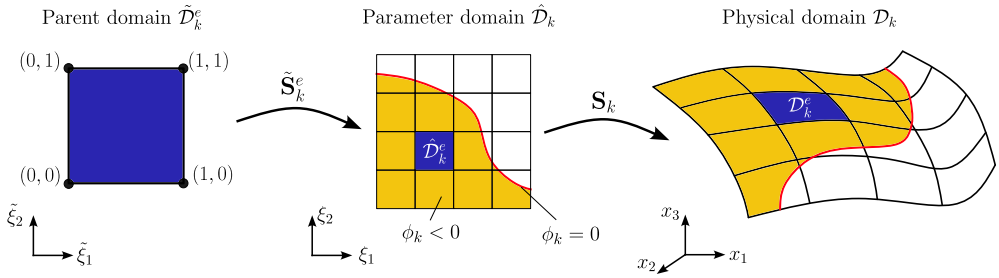

Fig. 3: Mapping an element into the parent space.

Let us now we consider a level set function ϕ_k to describe the material phase $\Omega_k \subset \mathcal{D}_k$. As illustrated in Figure 4, the level set $\phi_k = 0$ implicitly defines a set of trimming curves, which delineates the interface between the strong and weak phases. However, in classical trimming problems in isogeometric analysis, the trimming curve

is given directly by a parameterized curve. In this paper, we propose to adapt these techniques, as presented in Kim et al. (2009), to the level set method by computing in each element the parametric curve defined by the level set zero.

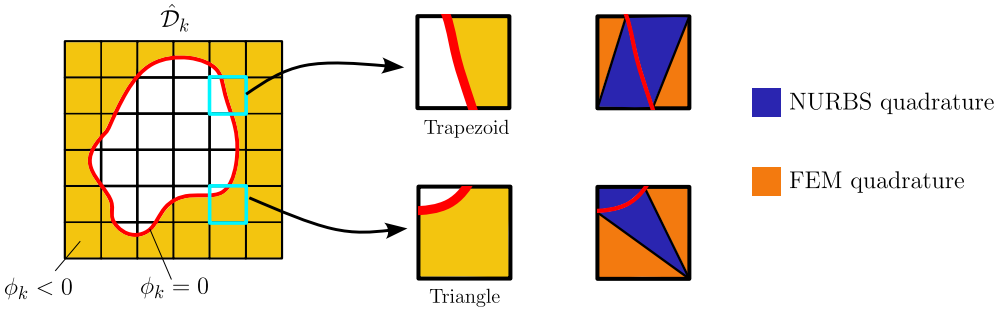

Fig. 4: The types of cut elements considered: it is assumed that each element in the parametric space is cut into one of the two kinds: a trapezoid or a triangle shape. These elements are subdivided into four triangles, as depicted on the right. The triangles that intersect the interface, displayed in blue, are integrated with NURBS-enhanced quadrature points, whereas the remaining triangles, represented in orange, are integrated with traditional quadrature points for triangles in FEM.

The trimming procedure assumes that the elements are cut by the level set zero into two configurations, as shown in Figure 4. The trimmed elements are further subdivided into curved and polygonal triangles. Triangles with straight edges are integrated using traditional FEM quadrature points. In contrast, triangles with a curved side are transformed through successive mappings into a reference quadrilateral element, where they can be integrated using complete NURBS-enhanced quadrature points. This mapping procedure is detailed further in Figure 5.

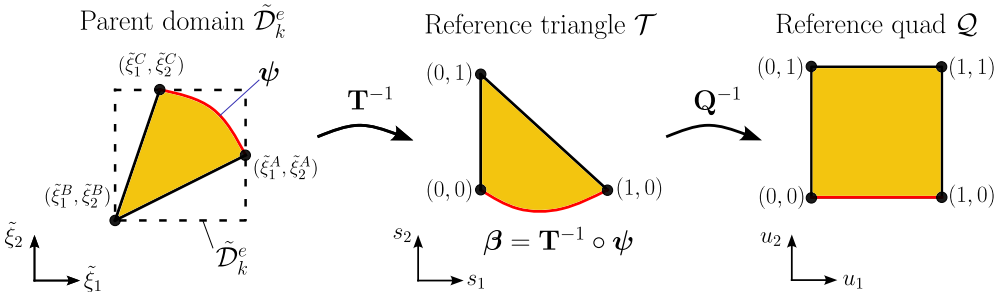

Fig. 5: Transformation of a curved triangle into a reference rectangle

Initially, a curved triangle, denoted $\tilde{\mathcal{D}}_k^e$, in the parent domain is mapped into a reference triangle $\mathcal{T}$ via a $\mathbf{T}$ transformation analogous to those used in FEM. This mapping is defined as follows:

$$\mathbf{T}(s_1, s_2) = \begin{bmatrix} \tilde{\xi}_1^A \\ \tilde{\xi}_2^A \end{bmatrix} + \begin{bmatrix} \tilde{\xi}_1^C - \tilde{\xi}_1^A & \tilde{\xi}_1^B - \tilde{\xi}_1^A \\ \tilde{\xi}_2^C - \tilde{\xi}_2^A & \tilde{\xi}_2^B - \tilde{\xi}_2^A \end{bmatrix} \begin{bmatrix} s_1 \\ s_2 \end{bmatrix} \tag{18}$$

Note also that this transformation only maps the corners of the curved triangle to a reference triangle. The curved edge of the original triangle, given by the parametric denoted $\boldsymbol{\psi} : [0, 1] \to \tilde{\mathcal{D}}_k^e$, is mapped to another parametric curve, denoted $\boldsymbol{\beta}$, which is expressed by $\boldsymbol{\beta} = \mathbf{T}^{-1} \circ \boldsymbol{\psi}$. Furthermore, the Jacobian of the transformation $\mathbf{T}$ is straightforwardly calculated as

$$J_{\mathbf{T}} = \begin{vmatrix} \frac{\partial \tilde{\xi}_1}{\partial s_1} & \frac{\partial \tilde{\xi}_1}{\partial s_2} \\ \frac{\partial \tilde{\xi}_2}{\partial s_1} & \frac{\partial \tilde{\xi}_2}{\partial s_2} \end{vmatrix} = \begin{vmatrix} \tilde{\xi}_1^C - \tilde{\xi}_1^A & \tilde{\xi}_1^B - \tilde{\xi}_1^A \\ \tilde{\xi}_2^C - \tilde{\xi}_2^A & \tilde{\xi}_2^B - \tilde{\xi}_2^A \end{vmatrix} \tag{19}$$

Next, the reference triangle is transformed into a reference rectangle using a generalized Duffy transform. The mapping is expressed in terms of the curve $\boldsymbol{\beta}(u_1) = (\beta_1(u_1), \beta_2(u_1))$ as

$$\mathbf{Q}(u_1, u_2) = \begin{bmatrix} \beta_1(u_1)(1 - u_2) \\ \beta_2(u_1)(1 - u_2) + u_2 \end{bmatrix} \tag{20}$$

It is noteworthy that this transformation degenerates the entire edge $[0, 1] \times \{1\}$ into a single point at $(0, 1)$. Consequently, it is imperative to refrain from utilising quadrature schemes with integration points situated on this edge. Moreover, when computing the Jacobian of the transformation $\mathbf{Q}$, one finds that

$$J_{\mathbf{Q}} = \begin{vmatrix} \frac{\partial s_1}{\partial u_1} & \frac{\partial s_1}{\partial u_2} \\ \frac{\partial s_2}{\partial u_1} & \frac{\partial s_2}{\partial u_2} \end{vmatrix} = \begin{vmatrix} \frac{\partial \beta_1}{\partial u_1}(u_1)(1 - u_2) & -\beta_1(u_1) \\ \frac{\partial \beta_2}{\partial u_1}(u_1)(1 - u_2) & 1 - \beta_2(u_1) \end{vmatrix} \tag{21}$$

Note that in the particular case of triangles with straight edges, the transformation $\mathbf{Q}$ is referred to as the Duffy transformation. In this case, the curve $\boldsymbol{\beta}$ is expressed $\boldsymbol{\beta}(u_1) = (u_1, 0)$, which implies that the Jacobian is given by $J_{\mathbf{Q}} = |1 - u_2|$.

Let us now consider how to obtain the curve $\boldsymbol{\psi} : [0, 1] \to \tilde{\mathcal{D}}_k^e$ on a trimmed element, given a level set function. Our solution relies on local polynomial interpolation, which is a simple and robust choice. Given that the elements are assumed to be cut in triangular and trapezoidal configurations (see Figure 4) and that level set functions are sufficiently regular at the element level, polynomial interpolation up to degree three has proven sufficient for this application, as confirmed by numerical practice. For higher orders of interpolation, polynomial approximation has oscilatory behavior, in which case other types of curve fitting methods should be considered, see for instance Costa et al. (2018) for NURBS-based fitting algorithms.

Based on a chosen integer polynomial degree $N - 1$, a real-valued interval is determined as either one of the vertical or horizontal axis as the abscissa of the polynomial

approximation of the curve. The abscissa, denoted $\iota \in \{1,2\}$, is determined based on the following criterion:

$$\iota = \underset{\alpha\in\{1,2\}}{\arg\max} |\xi_\alpha^A - \xi_\alpha^C| \tag{22}$$

Let $\{(\mathcal{I}_k^e)_n\}_{n=1}^N$ be a uniformly distributed local discretization of the abscissa of the element e in which each component is defined by:

$$(\mathcal{I}_k^e)_n = \frac{n-1}{N-1}\tilde{\xi}_\iota^A + \left(1 - \frac{n-1}{N-1}\right)\tilde{\xi}_\iota^C \quad \forall n \in [\![1, N]\!] \tag{23}$$

Then, we introduce the ordinate points of the local interpolation with the sequence $\{(\mathcal{Y}_k^e)_n\}_{n=1}^N$ by computing the intersection of the level set function ϕ_k at the points of the local abscissa discretization. Hence, the components $(\mathcal{Y}_k^e)_n$ are given by the solution of the following problem for each $n \in [\![1, N]\!]$:

$$\text{Find } (\mathcal{Y}_k^e)_n \in [0,1] \quad \text{such that} \quad \begin{cases} \hat{\phi}_k\left(\tilde{\mathbf{S}}_k^e\big((\mathcal{I}_k^e)_n, (\mathcal{Y}_k^e)_n\big)\right) = 0 & \text{if } \iota = 1 \\ \hat{\phi}_k\left(\tilde{\mathbf{S}}_k^e\big((\mathcal{Y}_k^e)_n, (\mathcal{I}_k^e)_n\big)\right) = 0 & \text{if } \iota = 2 \end{cases} \tag{24}$$

Finally, the curve $\boldsymbol{\psi} : [0,1] \to \hat{\mathcal{D}}_k^e$ is computed with the polynomial π_k^e that interpolates the points $\{((\mathcal{I}_k^e)_n, (\mathcal{Y}_k^e)_n)\}_{n=1}^N$ by:

$$\boldsymbol{\psi}(u) = \begin{cases} (\eta_u, \pi_k^e(\eta_u)) \text{ if } \iota = 1 \\ (\pi_k^e(\eta_u), \eta_u) \text{ if } \iota = 2 \end{cases}, \quad \text{with } \eta_u = \xi_\iota^A(1-u) + \xi_\iota^C u \tag{25}$$

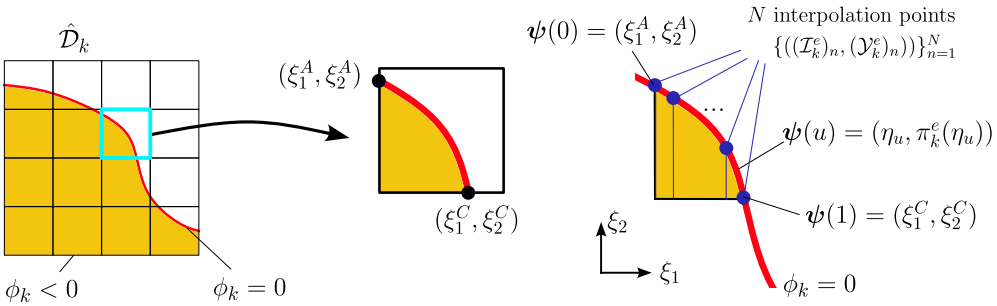

Fig. 6: Approximation of the interface using local polynomial interpolation of the curve $\phi_k = 0$.

At this juncture, it is possible to evaluate the integral of an arbitrary function $h : \tilde{\mathcal{D}}_k^e \to \mathbb{R}$ over the trimmed element $\tilde{\mathcal{D}}_k^e$ as the sum of the contributions of each triangular element obtained by the trimming procedure. After a change of coordinates to their respective reference rectangular element and taking into account the Jacobian of this composed transformation, this integral is expressed as follows:

$$\int_{\tilde{\mathcal{D}}_k^e} h(\tilde{\xi}_1, \tilde{\xi}_2)\, \mathrm{d}\tilde{\xi}_1\, \mathrm{d}\tilde{\xi}_2 = \sum_c \int_{\mathcal{Q}_c} (h \circ \mathbf{T}_c \circ \mathbf{Q}_c)(u_1, u_2) |\det J_{\mathbf{T}_c \circ \mathbf{Q}_c}|\, \mathrm{d}u_1\, \mathrm{d}u_2 \tag{26}$$

where the indices c are the different curved and polygonal triangles that partition the element $\tilde{\mathcal{D}}_k^e$.

As for the integration of the untrimmed elements, we retain the reduced quadrature points proposed in Adam et al. (2020), which allows for reducing numerical locking effects on thick shells because of the high regularity of the NURBS basis functions. By denoting n_{GPC} the number of Gaussian points for exact integration of NURBS of degree d, the number of Gaussian points in the reduced integration in each direction is $n_{GPC} - 1$ for the interior elements and $n_{GPC} - reg - 1$ for the boundary elements, where reg is the desired regularity ($0 < reg < d$). In Figure 8 we illustrate the choice of integration points for cubic NURBS and regularity C^2, the main type of elements employed in the numerical practice of the present study.

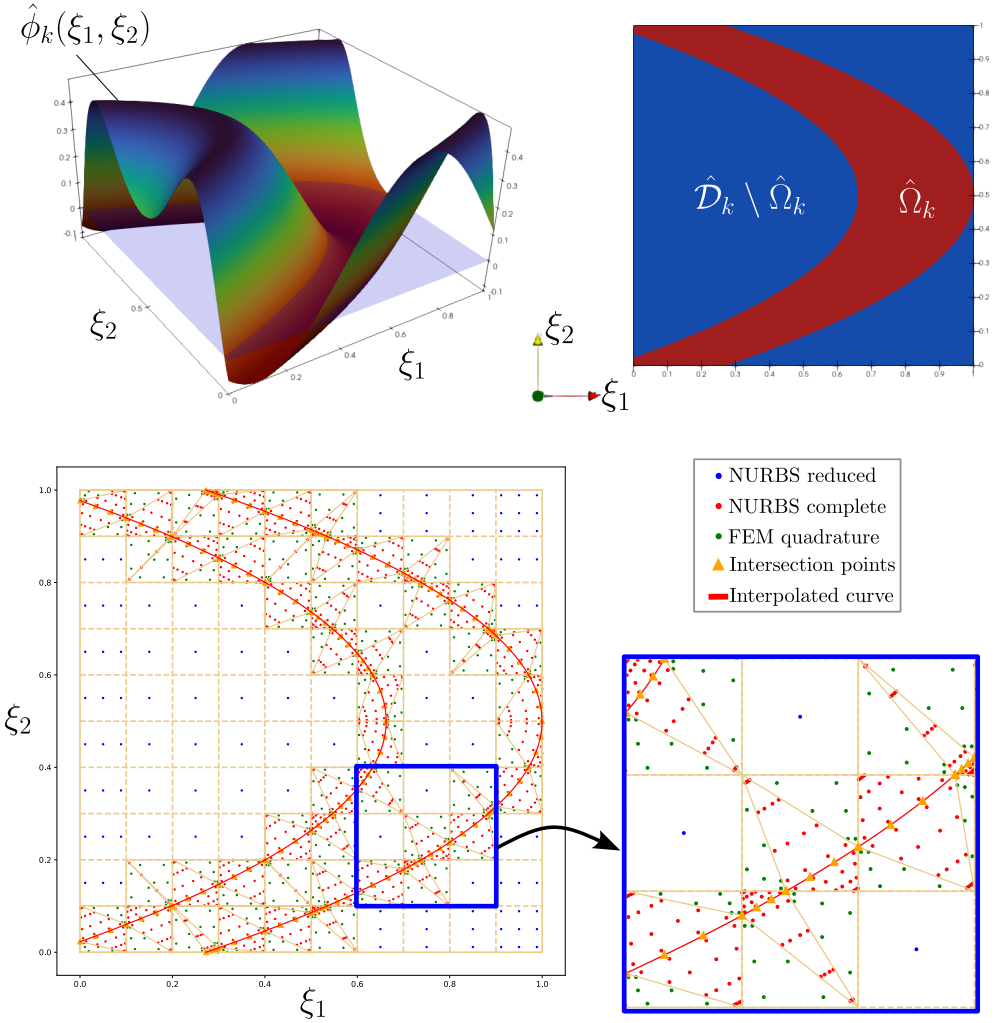

Fig. 7: Trimming procedure with a level set function. In this particular example, the plot of a level set function given by $\hat{\phi}(\xi_1, \xi_2) = -\sin(5.5\xi_1 + (4\xi_2 - 2)^2 - 3) + 0.6$ is displayed in the top left. The top right panel illustrates how this function implicitly defines the parametric material phase $\hat{\Omega}$ by the negative values of ϕ. The bottom panel illustrates the integration points for each element when using cubic NURBS with C^2 regularity. The trimmed elements are subdivided into a set of curved and polygonal triangles. The curved triangles utilize complete Gaussian quadrature points for NURBS (shown in red), while the straight-sided triangles employ Legendre-Gauss integration points for classical finite element method (shown in green). Additionally, the untrimmed elements use reduced integration quadrature (shown in blue). A portion of the parametric domain is depicted in greater detail, where one can observe the selection of interpolation points utilized, as well as the resulting interpolating trimming curve of degree 3.

5 IGA representation of the material level set

Let us address the problem of the linear elastic Reissner-Mindlin shell on a multi-patch shape $\Omega \subset \mathcal{D}$, characterized by a level set function $\phi = \{\phi_k\}_{k=1}^K$. Since we are considering a two phase approach, we introduce two constitutive tensors: C^{ijrs} to model the material behavior of the strong phase and $\tilde{C}^{ijrs}$ for that of the weak phase. In each patch, the effective material behavior is given by the constitutive tensor A^{ijrs}, which varies within the domain $\mathcal{D}_k$ as a function the level set ϕ_k:

$$A^{ijrs}(\phi_k) = \begin{cases} C^{ijrs} & \text{in } \Omega_k \qquad \textit{(strong phase, } \phi_k < 0\textit{)} \\ \tilde{C}^{ijrs} & \text{in } \mathcal{D}_k \setminus \Omega_k \qquad \textit{(weak phase, } \phi_k > 0\textit{)} \end{cases} \tag{27}$$

As a consequence, the stress tensor is also expressed with a dependency on the level set function and the constitutive tensors of the strong and weak phases:

$${\sigma_{\phi_k}}^{ij} = \underbrace{\left((C^{ijrs} - \tilde{C}^{ijrs})\mathbb{1}_{\Omega_k} + \tilde{C}^{ijrs}\right)}_{A^{ijrs}(\phi_k)} \varepsilon_{rs}. \tag{28}$$

where $\mathbb{1}_{\Omega_k} : \mathcal{D}_k \to \{0, 1\}$ denotes the indicator function defined as $\mathbb{1}_{\Omega_k}(\boldsymbol{x}) = 1$ when $\boldsymbol{x} \in \Omega_k$ and $\mathbb{1}_{\Omega_k}(\boldsymbol{x}) = 0$ otherwise.

Let us now formulate the weak formulation of the linear elasticity in the space $H^1_D(\mathcal{D})$, as introduced in equation (8), which we now decompose into local H^1 spaces:

$$H^1_D(\mathcal{D}_k) = \{\mathbf{v}_k = (\mathbf{v}_k^U, \mathbf{v}_k^R) \in H^1(\mathcal{D}_k) \times H^1(\mathcal{D}_k) : \mathbf{v}_k^U|_{\partial\mathcal{D}_D^U} = \mathbf{0}, \quad \mathbf{v}_k^R|_{\partial\mathcal{D}_D^R} = \mathbf{0}\} \tag{29}$$

The Reissner-Mindlin shell formulation, as presented in problem (9), is also rewritten with a dependency on the level set functions. For this purpose, we introduce for each patch the local (continuous and coercive) bilinear form $a_k : H^1_D(\mathcal{D}_k) \times H^1_D(\mathcal{D}_k) \to \mathbb{R}$ and a (continuous) linear form $L_k : H^1_D(\mathcal{D}_k) \to \mathbb{R}$ by:

$$\begin{aligned} a_k(\mathbf{u}_k, \mathbf{v}_k) &= \int_{V_k} \sigma_{\phi_k}(\mathbf{u}_k) : \varepsilon(\mathbf{v}_k) \, \mathrm{d}V_k = \int_{[-\frac{\epsilon}{2}, \frac{\epsilon}{2}] \times \hat{\mathcal{D}}_k} \sigma_{\phi_k}(\mathbf{u}_k) : \varepsilon(\mathbf{v}_k) |\det J_{\boldsymbol{\mathcal{V}}_k}| \, \mathrm{d}\hat{\mathcal{D}}_k \, \mathrm{d}\xi_3 \\ L_k(\mathbf{v}_k) &= \int_{V_k} \left(\mathbf{f}_k^V \cdot \mathbf{v}_k\right) \mathbb{1}_{\Omega_k} \, \mathrm{d}V_k + \int_{\mathcal{D}_k} \left(\mathbf{f}_k^S \cdot \mathbf{v}_k\right) \mathbb{1}_{\Omega_k} \, \mathrm{d}\mathcal{D}_k + \int_{\partial\mathcal{D}_N} (\mathbf{v}_k^U \cdot \mathbf{g}_k + \mathbf{v}_k^R \cdot \mathbf{m}_k) \, \mathrm{d}\gamma \end{aligned} \tag{30}$$

where $J_{\boldsymbol{\mathcal{V}}_k}$ is the Jacobian matrix associated with transformation $\boldsymbol{\mathcal{V}}_k$ in equation (2).

5.1 Interface continuity with an augmented Lagrangian formulation

In a previous paper Hübner Scherer et al. (2024), we presented an IGA-based topology optimization technique for the compliance, which used a penalty approach to ensure

the continuity of the fields at the interfaces γ_{kl}. In the present study, we extend this formulation to an augmented Lagrangian formulation, as developed in Adam et al. (2020), which we briefly summarize here for the sake of completeness. This approach is more robust from an algorithmic standpoint, as it is less dependent on the choice of the penalty parameter. For further details on the mathematical formulation of the augmented Lagrangian approach for domain decomposition on non-matching discretizations, we direct the reader to Tallec and Sassi (1995).

We consider now the displacements $\mathbf{u}^V$ in the volume defined by a NURBS approximation. Denoting $\mathbf{U}_B$ the displacement and $\mathbf{r}_B$ the rotation associated with the control point $\mathbf{X}_B$, this displacement $\mathbf{u}^V$ is written as:

$$\mathbf{u}^V(\xi_1,\xi_2,\xi_2) = \mathbf{u}^{\mathcal{D}}(\xi_1,\xi_2)+\xi_3\mathbf{r}(\xi_1,\xi_2)\times\mathbf{a}_3(\xi_1,\xi_2) = \sum_{B=1}^{n_1\cdot n_2} R_B\left(\mathbf{U}_B + \xi_3\mathbf{r}_B\times\mathbf{a}_3(\xi_1,\xi_2)\right). \tag{31}$$

It follows that the finite dimensional space $U_{k,h} \subset H^1_D(\mathcal{D}_k)$ of discretization is generated by the NURBS functions with:

$$U_{k,h} = \left\{\mathbf{v}_k = \hat{\mathbf{v}}_k \circ \mathbf{S}_k^{-1} \quad \text{with } \hat{\mathbf{v}}_k \in \bigotimes_{\alpha\in\{1,2\}} \mathcal{R}(d_{k_\alpha},\Xi_{k_\alpha})\right\}, \tag{32}$$

where $\mathcal{R}(d_{k_\alpha},\Xi_{k_\alpha})$ is the space of NURBS functions defined on the patch k of degree d_{k_α} and knot vector Ξ_{k_α} in the direction $\alpha \in \{1,2\}$.

Denoting tr_{kl} as the boundary trace operator along the internal interface γ_{kl}, we introduce the bilinear forms b_{kl} and c_{kl} to ensure continuity across the interface γ_{kl}:

$$\begin{aligned} b_{kl} &: H^1_D(\mathcal{D}_k)\times H^1_D(\mathcal{D}_l) \to \mathbb{R}, \qquad (\mathbf{u}_k,\mathbf{v}_k) \mapsto \int_{\gamma_{kl}} (\mathrm{tr}_{kl}\mathbf{u}_k - \mathrm{tr}_{lk}\mathbf{u}_l)(\mathrm{tr}_{kl}\mathbf{v}_k - \mathrm{tr}_{lk}\mathbf{v}_l)\,\mathrm{d}\gamma_{kl} \\ c_{kl} &: L^2(\gamma_{kl})^2 \times L^2(\gamma_{kl})^2 \to \mathbb{R}, \qquad (\boldsymbol{\lambda}_{kl},\mathbf{u}_k) \mapsto \int_{\gamma_{kl}} \boldsymbol{\lambda}_{kl}\cdot\mathbf{u}_{kl}\,\mathrm{d}\gamma_{kl} \end{aligned} \tag{33}$$

The augmented Lagrangian approach employs Lagrange multipliers to weakly impose C^0 continuity at the interfaces between the patches in a slave-master setting. This approach consists of a combination of the penalized approach and mortar (or dualized) methods, which respectively correspond in this formulation to the bilinear forms b_{kl} and c_{kl}. It is particularly suitable for industrial applications due to its capability to manage complex multi-patch systems without the need for conformity conditions at the interfaces, such as matching knot vectors or degrees.

As discussed in Adam et al. (2020), the selection of the space of the Lagrange multipliers is of pivotal importance for the proof of the inf-sup stability condition and for the provision of an adequate approximation of the dual space. A suitable discrete approximation $M_{kl,h} = M_{lk,h} \subset L^2(\gamma_{kl})^2$ of this space is defined as follows:

$$M_{kl,h} = \{\mathbf{w} \in \mathrm{tr}_{kl}U_{s(kl),h}, \quad \text{with } \mathbf{w}_B = \mathbf{0} \text{ at all corners of } \mathcal{D}_{s(kl)}\} \tag{34}$$

where denotes $s(kl)$ a restriction to the arbitrarily chosen slave edge of the interface γ_{kl}.

Then, the problem of linear elasticity on the elastic Reisnner-Mindlin multi-patch shell is to find the discrete displacements $\mathbf{u} = \{\mathbf{u}_k\} \in \prod_k U_{k,h}$ and the Lagrange multipliers $\{\boldsymbol{\lambda}_{kl}\} \in \prod_k M_{k,h}$ such that the elastic equilibrium equation is satisfied:

$$\begin{aligned} \sum_k a_k(\mathbf{u}_k, \mathbf{v}_k) + \sum_{k>l} \varrho_{kl}^{LE} b_{kl}(\mathbf{u}_k, \mathbf{v}_k) + \sum_{k>l} c_{kl}(\boldsymbol{\lambda}_{kl}, \mathrm{tr}_{kl}\mathbf{u}_k - \mathrm{tr}_{kl}\mathbf{u}_l) &= \sum_k L_k(\mathbf{v}_k) \\ \sum_{k>l} c_{kl}(\boldsymbol{\mu}_{kl}, \mathrm{tr}_{kl}\mathbf{u}_k - \mathrm{tr}_{kl}\mathbf{u}_l) &= 0 \end{aligned} \tag{35}$$

for arbitrary test functions $\{\mathbf{v}_k\} \in \prod_k U_{k,h}$ and Lagrange multipliers $\{\boldsymbol{\mu}_{kl}\} \in \prod_k M_{k,h}$. In this problem, ϱ_{kl}^{LE} is a large penalty factor for the interface γ_{kl} associated with the linear elasticity problem (LE).

6 Shape optimization problem

The optimization problem under consideration seeks to determine the material distribution within the multi-patch mid-surface $\mathcal{D}$, subject to given loading and boundary conditions. Accordingly, we impose a constraint ensuring that the region $\partial\mathcal{D}_N$ remains unchanged throughout the evolution of the shape Ω. Additionally, we denote a region $\partial\mathcal{D}_D$ where the shell is subject to constraints on displacement or rotation, while allowing the shape to evolve freely within this region. Thus, the set of admissible shapes can be defined as follows:

$$\mathcal{U}_{ad} = \{\Omega \subset \mathcal{D} : \partial\Omega_N = \partial\mathcal{D}_N \text{ and } \partial\Omega_D \subset \partial\mathcal{D}_D\} \tag{36}$$

We propose the study of a general cost function $\mathcal{J} : \mathcal{P}(\mathcal{D}) \to \mathbb{R}$ that aims to minimize the volume of the shape Ω while simultaneously taking into consideration stress criteria in two distinct ways. The first is to consider the L^p norm of the von Mises stress, which allows for reducing the values of stress on the whole shape. The second is a pointwise penalization of the von Mises stress greater than the yield stress $\sigma_Y > 0$ of the material. This objective function is expressed as:

$$\mathcal{J}(\Omega) = \sum_k \underbrace{\int_{\Omega_k} \mathbb{1}_{\Omega_k} \,\mathrm{d}V_k}_{\text{volume}} + \Lambda^P \underbrace{\left(\sum_k \int_{V_k} (\sigma_{vm}(\mathbf{u}))^p \,\mathrm{d}V_k \right)^{\frac{1}{p}}}_{L^p \text{ norm of von Mises stress}} + \Lambda^Q \sum_k \underbrace{\int_{\Omega_k} \Phi_q\left(\frac{\sigma_{vm}(\mathbf{u})^2}{\sigma_Y^2} \right) \mathrm{d}V_k}_{\text{stress constraint}} \tag{37}$$

where $\Lambda^P, \Lambda^Q > 0$ are two fixed scale factors chosen arbitrarily, and $\mathbf{u} = \{\mathbf{u}_k\} \in \prod_k H_D^1(\mathcal{D}_k)$ is the multi-patch displacement field, solution of linear elasticity problem (35). We remark that both the p-norm and the displacement $\mathbf{u}$ itself depend on the shape Ω and the level set functions $\{\phi_k\}$.

The stress constraint is addressed in accordance with the methodology proposed by Amstutz (2010) to permit the enforcement of the condition $\frac{\sigma_{vm}}{\sigma_Y} < 1$ throughout the domain. This is accomplished by the penalization function Φ_q, depicted in Figure 8. In order for the aforementioned constraint to be satisfied, it is necessary that both the integer parameter q and the penalty factor Λ^Q are sufficiently large.

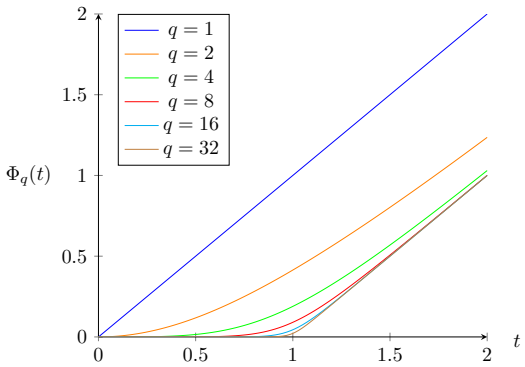

Fig. 8: Penalization function from Amstutz and Novotny (2010) used to ensure the condition $\frac{\sigma_{vm}}{\sigma_Y} < 1$.

The optimization problem aims to find the optimal shape $\Omega^* \in \mathcal{U}_{ad}$ such that:

$$\begin{aligned} &\mathcal{J}(\Omega^*) = \inf_{\Omega \in \mathcal{U}_{ad}} \mathcal{J}(\Omega), \\ &\text{subject to (35)} \end{aligned} \tag{38}$$

It is noteworthy that the p-norm in problem (38) can be equivalently formulated in terms of the yield stress $\sigma_Y > 0$ as proposed in Wang and Li (2013). In this formulation, the p-norm term in the cost function in equation (37) is replaced by $\left\| \frac{\sigma_{vm}(\mathbf{u})}{\sigma_Y} \right\|_{L^p(\mathcal{D})}$, which allows to view the cost function as a penalization of stresses greater than the yield stress. The integer p can therefore be selected to enhance the penalization effect. Additionally, we also remark that the p-norm can also be interpreted as an approximation of the maximum stress, since it tends to the essential supremum of σ_{vm} as $p \to \infty$.

This problem is solved using the level set method detailed in Section 3. The velocity field $\boldsymbol{v}(\boldsymbol{x}, t)$ of the Hamilton-Jacobi in equation (17) is coupled with the descent direction of the cost function in equation (37). This descent direction is derived through a regularization process applied to the shape derivative of the objective function $\mathcal{J}$. In the present study, we present a *tensor representation* for the L^p norm shape derivative, also called *distributed shape derivative* (see Laurain, Antoine and Sturm, Kevin (2016)), demonstrated through a similar mathematical approach as seen for the compliance in Laurain (2018).

Regularization field on the tangent bundle. The evolution of the material points within the domain is governed by a velocity field denoted as $\boldsymbol{\theta}$, also called the *regularization field*, which corresponds to the descent direction of the cost function. It is imperative for this field to satisfy to two crucial conditions. First, we mandate that the field $\boldsymbol{\theta}$ is restricted to the tangent bundle of $\mathcal{D}$ to ensure the preservation of the thickness of the shell. Second, at the boundary points, the of the field direction pointing outward from the shell is enforced to be zero, thus guaranteeing that the shape remains contained within the optimization domain $\mathcal{D}$.

Following these conditions, let us introduce the function space $\Theta(\mathcal{D}_k)$ of the regularization fields:

$$\Theta(\mathcal{D}_k) = \Big\{ \boldsymbol{\vartheta}_k \in (H^1(\mathcal{D}_k))^3 : \quad \boldsymbol{\vartheta}_k \cdot \mathbf{a}^3 = 0 \text{ in } \mathcal{D}_k \text{ and } \boldsymbol{\vartheta}_k \cdot \mathbf{t}_N = 0 \text{ on } \partial\mathcal{D}_k \setminus \bigcup_{\substack{l=1 \\ l \neq k}}^{K} \gamma_{kl} \Big\}, \tag{39}$$

recalling that $\mathbf{t}_N \in T(\mathcal{D}_k)$ is the unit outward normal to $\partial\mathcal{D}_k$ in the tangent space and $\mathbf{a}^i$ denotes the contravariant basis in the mid-surfaces, obtained by $\mathbf{a}_i \cdot \mathbf{a}^j = \delta_i^j$.

To obtain the tensor representation of the shape derivative, we consider a Langragian approach where we follow the evolution of the points in $\mathbb{R}^3$ given a velocity field $\boldsymbol{\theta} \in \Theta(\mathcal{D}_k)$. To track the position of a point $\boldsymbol{x}_0 \in \mathbb{R}^3$ in the course of a pseudo-time $t \in [0, \tau]$, we introduce the mapping $\boldsymbol{\Upsilon}_t : \mathbb{R}^3 \to \mathbb{R}^3$, defined by $\boldsymbol{\Upsilon}_t = \boldsymbol{x}(t)$ where $\boldsymbol{x}(t) : [0, \tau] \to \mathbb{R}^3$ is the solution of the ODE:

$$\frac{\mathrm{d}\boldsymbol{x}}{\mathrm{d}t}(t) = \boldsymbol{\theta}(\boldsymbol{x}) \quad \text{ for } t \in [0, \tau] \text{ and } \boldsymbol{x}(0) = \boldsymbol{x}_0. \tag{40}$$

Using the map $\boldsymbol{\Upsilon}_t$, we track the evolution of a given initial shape Ω in terms of the pseudo-time with:

$$\Omega_t = \boldsymbol{\Upsilon}_t(\Omega). \tag{41}$$

Let us introduce the definition of the shape derivative as in Laurain, Antoine and Sturm, Kevin (2016).

Definition *1 (Shape derivative).* Let $J : \mathcal{P}(\mathcal{D}) \to \mathbb{R}$ be a shape function.

(i) The Eulerian semiderivative of J at Ω in direction $\boldsymbol{\theta} \in \Theta(D)$, when the limit exists, is defined by

$$\mathrm{d}J(\Omega; \theta) := \lim_{t \searrow 0} \frac{J(\Omega_t) - J(\Omega)}{t}$$

(ii) J is shape differentiable at Ω if it has a Eulerian semiderivative at Ω for all $\boldsymbol{\theta} \in \Theta(D)$ and the mapping

$$J'(\Omega) : \Theta(\mathcal{D}) \to \mathbb{R}, \qquad \theta \mapsto J'(\Omega)(\theta) = \mathrm{d}J(\Omega; \theta)$$

is linear and continuous, in which case $J'(\Omega)(\theta)$ is called the shape derivative at Ω in the direction of θ.

The shape derivative of the cost functional in equation (37) is already known from several works, see for instance Allaire and Jouve (2008); Picelli et al. (2018); Goo et al. (2016); Ho-Nguyen-Tan and Kim (2021). The expression of the shape derivative is given by a boundary integral, which is usually computed numerically as a volume integral by means of a Dirac function using the sign function (see Allaire et al. (2004), page 384). In the present paper, however, we propose an alternative formula that is instead expressed as an integral directly over the volume, using a *tensor representation*. We will show later that both formulations are equivalent.

Definition 2 *(Tensor representation).* Let $\Omega \in \mathcal{P}(\mathcal{D})$ be an open set. A shape differentiable function J admits a tensor representation of order 1 if there exists two tensors $F_\alpha \in L^\alpha(\mathcal{D}, \mathcal{L}^\alpha(\mathbb{R}^d, \mathbb{R}^d))$ with $\alpha = 0, 1$ such that

$$J'(\Omega)(\boldsymbol{\theta}) = \int_{\mathcal{D}} F_1 : \nabla \boldsymbol{\theta} + F_0 \cdot \boldsymbol{\theta} \, \mathrm{d}x.$$

Let us now consider how to derive the tensor representation of the shape derivative related to the cost functional in 37. For the sake of simplicity of notation during this derivation, let us consider the functional:

$$J(\Omega) := \int_\Omega f(Ae(\mathbf{u})) \, \mathrm{d}V, \tag{42}$$

where f is a given integrand function of the stress and A is a second order such that for any second order symmetric tensor χ we have $A\chi = 2\mu\chi + \lambda \mathrm{tr}\chi \, \mathrm{I}$. We have chosen to derive the expression depending on the function f so that the expression of of notation allows us to deal with a wider set of cost functionals and not only that of the special case of our interest, namely the norm L^p of the von Mises stress. In an ersatz approach, we also consider introducing the notation A_ϕ to extend the integral (42) over the shape Ω to the whole domain $\mathcal{D}$ by multiplying the original tensor A by a small factor $e > 0$ on the void phase:

$$A_\phi = A\mathbb{1}_\Omega + eA\mathbb{1}_{\mathcal{D}\setminus\Omega}. \tag{43}$$

6.1 Change of variables

Since we write our problems of interest in terms of weak formulations of an evolving shape Ω_t, we now consider applying a number of variable changes using the parameterization $\boldsymbol{\Upsilon}_t$ to rewrite all the problems in terms of the unchanged domain $\mathcal{D}$. Therefore, we will rewrite the cost function and the linear elasticity problem using the transformation $\boldsymbol{x} \mapsto \boldsymbol{\Upsilon}_t(\boldsymbol{x})$. For such purposes, let us consider the two definitions $\mathbf{u}^t := \mathbf{u}_t \circ \boldsymbol{\Upsilon}_t$ and $E(t, \mathbf{u}^t) := \varepsilon(\mathbf{u}_t) \circ \boldsymbol{\Upsilon}_t$. The idea is that $\mathbf{u}_t$ and $\varepsilon(\mathbf{u}_t)$ express the displacement field and strain tensor in the deformed configuration, i.e. in Ω_t, while $\mathbf{u}^t$ and $E(t, \mathbf{u}^t)$ express the same quantities but directly over the underformed shape $\mathcal{D}$.

Let us investigate the relationship between the derivatives of $\mathbf{u}^t$ and those of $\mathbf{u}_t$. By applying the chain rule on a composition, we get $\nabla \mathbf{u}^t = \nabla(\mathbf{u}_t \circ \boldsymbol{\Upsilon}_t) = \nabla \mathbf{u}_t \circ \boldsymbol{\Upsilon}_t \nabla \boldsymbol{\Upsilon}_t$. Subsequently, we can express $E(t, \mathbf{u}^t)$ in terms of $\nabla \mathbf{u}^t$ as:

$$\begin{aligned} E(t, \mathbf{u}^t) = \varepsilon(\mathbf{u}_t) \circ \boldsymbol{\Upsilon}_t &= \frac{1}{2}\left(\nabla \mathbf{u}_t \circ \boldsymbol{\Upsilon}_t + \nabla \mathbf{u}_t^T \circ \boldsymbol{\Upsilon}_t\right) \\ &= \frac{1}{2}\left(\nabla \mathbf{u}_t \circ \boldsymbol{\Upsilon}_t \left(\nabla \boldsymbol{\Upsilon}_t \nabla \boldsymbol{\Upsilon}_t^{-1}\right) + \nabla \mathbf{u}_t^T \circ \boldsymbol{\Upsilon}_t \left(\nabla \boldsymbol{\Upsilon}_t^T \nabla \boldsymbol{\Upsilon}_t^{-T}\right)\right) \\ &= \frac{1}{2}\left(\nabla \mathbf{u}^t \nabla \boldsymbol{\Upsilon}_t^{-1} + \nabla \boldsymbol{\Upsilon}_t^{-T} \left(\nabla \mathbf{u}^t\right)^T\right). \end{aligned} \tag{44}$$

By denoting $\delta(t) = |\det J_{\boldsymbol{\Upsilon}_t}|$ the determinant of the Jacobian of the transformation $\boldsymbol{\Upsilon}_t$, the cost function can be rewritten with this change of coordinates as:

$$J(\Omega) = \int_{\Omega_t} f(A\varepsilon(\mathbf{u}_t))\, \mathrm{d}V_t = \int_{\mathcal{D}} f(A_\phi E(t, \mathbf{u}^t))\delta(t)\, \mathrm{d}V \tag{45}$$

Similarly, the weak formulation of the linear elasticity problem, stated in equation (35), can be rewritten with the change of coordinates $\boldsymbol{x} \mapsto \boldsymbol{\Upsilon}_t(\boldsymbol{x})$ as:

$$\int_{\mathcal{D}} A_\phi E(t, \mathbf{u}^t) : E(t, \boldsymbol{v})\delta(t) = \int_{\partial \mathcal{D}_N} \boldsymbol{g} \cdot \boldsymbol{v} \tag{46}$$

6.2 Lagrangian approach

For the optimization problem in equation (38) we consider a Lagrangian approach. Let us then define the Lagrangian $\mathcal{L} : [0, \tau] \times H_D^1(\mathcal{D}) \times H_D^1(\mathcal{D}) \to \mathbb{R}$ as:

$$\mathcal{L}(t, \boldsymbol{v}, \boldsymbol{q}) = \int_{\mathcal{D}} f(A_\phi E(t, \boldsymbol{v}))\delta(t)\, \mathrm{d}V + \int_{\mathcal{D}} A_\phi E(t, \boldsymbol{v}) : E(t, \boldsymbol{q})\delta(t)\, \mathrm{d}V - \int_{\partial \mathcal{D}_N} \boldsymbol{g} \cdot \boldsymbol{q}\, \mathrm{d}s \tag{47}$$

We remark that the first term of the Lagrangian in 47 is related to the cost functional in 42. The two subsequent terms are that of the weak formulation computed in 46. Therefore, if we take $\mathbf{u}^t \in H_D^1(\mathcal{D})$ solution of the linear elasticity at time t over the domain Ω_t, we have that $\mathcal{L}(t, \mathbf{u}^t, \boldsymbol{q}) = J(\Omega_t)$ for any $\boldsymbol{q} \in H_D^1(\mathcal{D})$. Note that with this, one can compute the shape derivative with

$$J'(\Omega)(\boldsymbol{\theta}) = \frac{\mathrm{d}}{\mathrm{d}t}(\mathcal{L}(t, \boldsymbol{u}^t, \boldsymbol{q}))|_{t=0} \tag{48}$$

Additionally, notice that where we simplified the weak formulation in (35) since in our applications $\mathbf{f}^V$, $\mathbf{f}^S$, $\mathbf{m}$ are all zero across all patches.

6.2.1 The adjoint problem

The adjoint equation is obtained as an optimility condition, which is defined by the problem:

$$\text{Find } \boldsymbol{p} \in H^1_D(\mathcal{D}) \quad \text{such that} \quad \left\langle \frac{\partial \mathcal{L}(0, \mathbf{u}, \boldsymbol{p})}{\partial \boldsymbol{v}}, \boldsymbol{\varphi} \right\rangle = 0 \quad \forall \boldsymbol{\varphi} \in H^1_D(\mathcal{D}) \tag{49}$$

Hence, by differentiating the Lagrangian in equation (47) with respect to $\boldsymbol{v}$, one has that:

$$\left\langle \frac{\partial \mathcal{L}(0, \mathbf{u}, \boldsymbol{p})}{\partial \boldsymbol{v}}, \boldsymbol{\varphi} \right\rangle = \int_{\Omega_t} f'(AE(0, \mathbf{u})) : AE(0, \boldsymbol{\varphi}) \delta(0) \, \mathrm{d}V + \int_{\Omega_t} AE(0, \boldsymbol{\varphi}) : E(0, \boldsymbol{p}) \delta(0) \, \mathrm{d}V \tag{50}$$

We rearrange this equation using the fact that $\delta(0) = 1$ and $E(0, \boldsymbol{v}) = e(\boldsymbol{v})$ for $\forall \boldsymbol{v} \in H^1_D(\mathcal{D})$. To rearrange the order of terms in the double contracted product, we consistently use the property $D : BC = B^T D : C = DC^T : B$, for any second order tensors D, B and C. With these considerations, the adjoint problem can be stated as finding $\boldsymbol{p} \in H^1_D(\mathcal{D})$ such that:

$$\int_{\Omega} A\varepsilon(\boldsymbol{p}) : \varepsilon(\boldsymbol{\varphi}) \, \mathrm{d}V = -\int_{\Omega} Af'(A\varepsilon(\mathbf{u})) : \varepsilon(\boldsymbol{\varphi}) \, \mathrm{d}V \quad \forall \boldsymbol{\varphi} \in H^1_D(\mathcal{D}) \tag{51}$$

where f' designates the derivative of the function f with respect to the components of the tensor $A\varepsilon(\mathbf{u})$.

With an integration by parts, it can be shown (see Allaire and Jouve (2008) for instance) that the variational problem (51) is equivalent to the following strong formulation:

$$\begin{cases} -\mathrm{div}(A\varepsilon(\boldsymbol{p})) = \mathrm{div}\left(Af'(A\varepsilon(\mathbf{u}))\right) & \text{in} \quad \Omega \\ \boldsymbol{p} = \mathbf{0} & \text{in} \quad \partial\Omega_D \\ (A\varepsilon(\boldsymbol{p}))\mathbf{n} = -(Af'(A\varepsilon(\mathbf{u})))\mathbf{n} & \text{in} \quad \partial\Omega_N \cup \partial\Omega_0 \end{cases} \tag{52}$$

6.3 The shape derivative

In the context of the Lagrangian approach, one can compute the shape derivative using:

$$J'(\Omega)(\boldsymbol{\theta}) = \frac{\mathrm{d}}{\mathrm{d}t}(\mathcal{L}(t, \mathbf{u}^t, \boldsymbol{q}))\Big|_{t=0} = \frac{\partial}{\partial t}(\mathcal{L}(0, \mathbf{u}^0, \boldsymbol{p}^0)) \tag{53}$$

Hence, we differentiate the Lagrangian in (47) with respect to the pseudo-time:

$$
\begin{aligned}
J'(\Omega)(\boldsymbol{\theta}) = &\int_{\mathcal{D}} f'(A_\phi E(0,\mathbf{u})) : \partial_t A_\phi E(0,\mathbf{u})\delta(0) + \int_D A_\phi \partial_t E(0,\mathbf{u}) : E(0,\boldsymbol{p})\delta(0) \\
&+ \int_{\mathcal{D}} A_\phi E(0,\mathbf{u}) : \partial_t E(0,\boldsymbol{p})\delta(0) + \int_{\mathcal{D}} f(A_\phi E(0,\mathbf{u}))\mathrm{div}\boldsymbol{\theta} \\
&+ \int_{\mathcal{D}} A_\phi E(0,\mathbf{u}) : E(0,\boldsymbol{p})\mathrm{div}\boldsymbol{\theta}
\end{aligned} \tag{54}
$$

To simplify this expression, we make use of the fact that $E(0,\boldsymbol{v}) = e(\boldsymbol{v})$ for all $\boldsymbol{v} \in H^1_D(\mathcal{D})$. Combining this with equation (44), it holds for all $\boldsymbol{v} \in H^1_D(\mathcal{D})$ that:

$$
\partial_t E(0,\boldsymbol{v}) = \frac{-\nabla\boldsymbol{v}\nabla\boldsymbol{\theta} - \nabla\boldsymbol{\theta}^T\nabla\boldsymbol{v}^T}{2} \tag{55}
$$

Finally, using equation (55), one can simplify (54) into:

$$
J'(\Omega)(\boldsymbol{\theta}) = \int_{\mathcal{D}} F_1(\mathbf{u},\boldsymbol{p}) : \nabla\boldsymbol{\theta} \tag{56}
$$

where

$$
\begin{aligned}
F_1(\mathbf{u},\boldsymbol{p}) = &-\nabla\mathbf{u}^T A_\phi f'(A_\phi\varepsilon(\mathbf{u})) - \nabla\mathbf{u}^T A_\phi\varepsilon(\boldsymbol{p}) - \nabla\boldsymbol{p}^T A_\phi\varepsilon(\mathbf{u}) \\
&+ \left(f(A_\phi\varepsilon(\mathbf{u})) + A_\phi\varepsilon(\mathbf{u}) : \varepsilon(\boldsymbol{p})\right)\mathbf{I}
\end{aligned} \tag{57}
$$

where $\mathbf{I}$ is the second order identity tensor.

Note that we have found a tensor representation for the shape derivative expressed with a volume integral. However, this shape derivative is usually expressed Allaire and Jouve (2008); Picelli et al. (2018); Goo et al. (2016); Ho-Nguyen-Tan and Kim (2021) as the following boundary integral:

$$
J'(\Omega)(\boldsymbol{\theta}) = \int_{\partial\Omega} \boldsymbol{\theta}\cdot\boldsymbol{n}\left(f(A\varepsilon(\mathbf{u})) + A\varepsilon(\mathbf{u}) : \varepsilon(\boldsymbol{p})\right)\mathrm{d}s \tag{58}
$$

We will demonstrate the expression of the shape derivative as a volume integral in (56) is equivalent to that written as a boundary integral as in equation (58). For this propose, let us enunciate proposition from Laurain (2018).

Proposition *1 (Boundary to volume representation).* Let $\Omega \in \mathcal{P}(\mathcal{D})$ and assume $\partial\Omega$ is C^2. Suppose that the shape derivative of a cost functional J has a tensor representation as in definition (2). If F_0 and F_1 are of class $W^{1,1}$ in Ω and $\mathcal{D}\setminus\overline{\Omega}$, then we obtain the so-called boundary expression of the shape derivative:

$$
J'(\Omega)(\boldsymbol{\theta}) = \int_{\partial\Omega} v\boldsymbol{\theta}\cdot\boldsymbol{n}
$$

with $v := [(F_1^+ - F_1^-)\boldsymbol{n}]\cdot\boldsymbol{n}$, where + and - denote the restrictions of the tensor to Ω and $\mathcal{D}\setminus\overline{\Omega}$.

Let us now demonstrate that the expression of the shape derivative as a volume integral in (56) is equivalent to that written as a boundary integral as in equation (58). We have already established that the shape derivative in equation (56) is a tensor representation. Furthermore, by means of the proposition (1), we have that:

$$\begin{aligned} v &= [(F_1^+ - F_1^-)\boldsymbol{n}] \cdot \boldsymbol{n} = [(F(\mathbf{u},\boldsymbol{p}) - \mathbf{0})\boldsymbol{n}] \cdot \boldsymbol{n} \\ &= (-\nabla \mathbf{u}^T \underbrace{(Af'(Ae(\mathbf{u}))\boldsymbol{n} + Ae(\boldsymbol{p})\boldsymbol{n})}_{=0 \text{ on } \partial\Omega\setminus\partial\Omega_D} - \nabla \boldsymbol{p}^T \underbrace{Ae(\mathbf{u})\boldsymbol{n}}_{=0 \text{ on } \partial\Omega_0} + (f(Ae(\mathbf{u})) + Ae(\mathbf{u}) : e(\boldsymbol{p}))\,\mathbf{I}\boldsymbol{n}) \cdot \boldsymbol{n} \\ &= f(Ae(\mathbf{u})) + Ae(\mathbf{u}) : e(\boldsymbol{p}) \end{aligned}$$

In particular, the shape derivative of the cost function (37) can be obtained through a similar Lagrangian approach. It follows that this shape derivative can be expressed as

$$\mathcal{J}'(\Omega)(\boldsymbol{\vartheta}) = \sum_k \int_{\Omega_k} \text{div}\boldsymbol{\vartheta}_k + \sum_k \int_{\mathcal{D}_k} F_1(\mathbf{u}_k, \boldsymbol{p}_k) : \nabla \boldsymbol{\vartheta}_k, \tag{59}$$

where F_1 is computed with equation (57) and the adjoint problem (51), both taking the function $\sigma \mapsto f(\sigma)$ as

$$f(Ae(\mathbf{v}_k)) = \frac{\Lambda^P}{p}(\|\sigma_{vm}(\mathbf{u})\|_{L^p(\mathcal{D})})^{1-p}(\sigma_{vm}(\mathbf{v}_k))^p + \Lambda^Q \Phi_q\left(\frac{\sigma_{vm}(\mathbf{v}_k)^2}{\sigma_Y^2}\right) \tag{60}$$

6.4 The regularization problem

Let us introduce the finite dimensional funcional space $\Theta^h(\mathcal{D}_k) \subset \Theta(\mathcal{D}_k)$ of the regularization problem, where the fields $\{\boldsymbol{\theta}_k\}$ are approximated by NURBS basis functions:

$$\Theta^h(\mathcal{D}_k) = \left\{\boldsymbol{\vartheta} = \hat{\boldsymbol{\vartheta}} \circ \mathbf{S}_k^{-1} : \hat{\boldsymbol{\vartheta}} \in \bigotimes_{i \in [\![0,2]\!]} \mathcal{R}(d_{k_i}, \Xi_{k_i})\right\}, \tag{61}$$

recalling that $\mathcal{R}(d_{k_i}, \Xi_{k_i})$ is the set of rational B-splines function defined on the patch k of degree d_{k_i} and with the knot vector Ξ_{k_i} in the direction $i \in \{0,1,2\}$.

Considering an identification problem using a scalar product over $\Theta(\mathcal{D}_k)$, we can formulate the **single-patch case** problem, which is enunciated by the following variational problem:

$$\textit{Find} \quad \boldsymbol{\theta} \in \Theta^h(\mathcal{D}) \quad \textit{s.t.} \quad \int_V \nabla_{\mathcal{D}}\boldsymbol{\theta} : \nabla_{\mathcal{D}}\boldsymbol{\vartheta} = -\mathcal{J}'(\Omega)(\boldsymbol{\vartheta}) \quad \forall \boldsymbol{\vartheta} \in \Theta^h(\mathcal{D}) \tag{62}$$

This approach can easily be generalized to a **multi-patch case**, similarly to what has been proposed for the linear elasticity case in Hübner Scherer et al. (2024), by

means of a penalty approach. Therefore, the regularization problem aims to find the field $\boldsymbol{\theta} = \{\boldsymbol{\theta}_k\} \in \prod_k \Theta^h(\mathcal{D}_k)$ such that

$$\sum_k \int_{V_k} \nabla_{\mathcal{D}} \boldsymbol{\theta}_k : \nabla_{\mathcal{D}} \boldsymbol{\vartheta}_k + \sum_{k>l} \varrho_{kl}^R b_{kl}(\boldsymbol{\theta}_k, \boldsymbol{\vartheta}_k) = -\sum_k \mathcal{J}'(\Omega_k)(\boldsymbol{\vartheta}_k) \quad \forall \boldsymbol{\vartheta} = \{\boldsymbol{\vartheta}_k\} \in \prod_k \Theta^h(\mathcal{D}_k) \tag{63}$$

where ϱ_{kl}^R is a penalty factor for the interface γ_{kl} of the regularization problem. It is worth noting that the left-hand of the equation does not depend on the level set function, meaning it is the same for all iterations. Denoting $\mathbf{L}$ the resulting matrix related to this term, it is therefore possible to reuse the factorization of the $\mathbf{L}$, thereby considerably reducing computational cost.

In Figure 9, an example of non-conforming multi-patch system is illustrated demonstrating how the boundary conditions and the continuity of the fields are imposed in the borders of the patches. On the external boundaries, the regularization field $\boldsymbol{\theta} \in \prod_k \Theta(\mathcal{D}_k)$ satisfies the condition $\mathbf{t}_N \cdot \boldsymbol{\theta}_k = 0$ for $\forall k$. On th internal interface, the continuity of the fields is weakly imposed by the penalization b_{kl} of the problem 63.

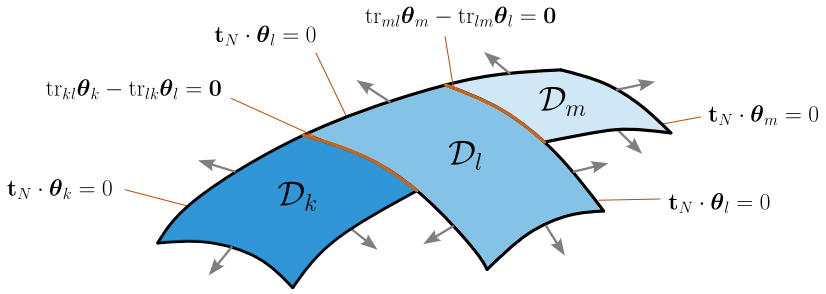

Fig. 9: Illustration of the boundary conditions and continuity conditions for a non-conforming multi-patch regularization problem.

The entire approach can be written in the format of a short algorithm, summarizing the different steps executed during the optimization. The technical details on the numerical implementation of this approach, along with its numerical results, are discussed next in Section 7. Further detail on the resolution of the regularization field on the tangent bundle and the resolution of the Hamilton-Jacobi on a non-conforming parameterized shell were presented in a previous work Hübner Scherer et al. (2024).

Algorithm 1 Stress-based topology optimization with isogeometric analysis

Input:
Multi-patch geometry using a set of NURBS parametrizations $\{\mathbf{S}_k\}$
Discretization grid $[\hat{G}_k]$ of the parametric domain $\hat{\mathcal{D}}_k$
Initial level set discretizations $[\phi_k]^{(0)}$
Parameters $\Lambda^P, \Lambda^Q, \sigma_Y, p, q$

Compute:
$\mathbf{L} \leftarrow$ Calculate and factorize the matrix of the regularization problem (63)
for $m \geq 0$ iterate until convergence **do**
  $\{\phi_k\}^{(m)} \leftarrow$ Compute the NURBS interpolation of $[\phi_k]^{(m)}$ over $[\hat{G}_k]$
  $\{\mathbf{u}_k\}^{(m)} \leftarrow$ Solve linear elasticity on the shell (35) with $\{\phi_k\}^{(m)}$
  $\{\boldsymbol{p}_k\}^{(m)} \leftarrow$ Solve adjoint problem on the shell (51) with $\{\mathbf{u}_k\}^{(m)}$ and $\{\phi_k\}^{(m)}$
  $\mathcal{J}^{(m)} \leftarrow$ Compute cost function
  if $m == 0$ **or** $\mathcal{J}^{(m)} < \mathcal{J}^{(m-1)}$ **then**
    $\mathcal{J}' \leftarrow$ Compute shape derivative using (59)
    $\{\boldsymbol{\theta}_k\}^{(m)} \leftarrow$ Solve regularization (63) with $\mathbf{L}$ and new right-hand term $\mathcal{J}'$
  else
    Decrease Δt of Hamilton-Jacobi
    Set $\{\boldsymbol{\theta}_k\}^{(m)} \leftarrow \{\boldsymbol{\theta}_k\}^{(m-1)}$
  end if
  $[\phi_k]^{(m+1)} \leftarrow$ Solve evolution equation (17) with $\{\boldsymbol{\theta}_k\}^{(m)}$, $\{\phi_k\}^{(m)}$ and Δt
end for

7 Numerical results

The numerical results presented in this section were obtained using a Python-based implementation of the algorithm (1). The just-in-time compiler from the *numba* Lam et al. (2015) was used to approach the speed of C or Fortran. The PyPardiso package Schenk et al. (2000) was employed to efficiently solve linear systems and perform LU factorization. Furthermore, the *numba* package was utilized for fast spline evaluations based on the approach outlined in Dierckx (1994).

Throughout this study, we tackled non-dimensionalized problems with a Poisson's ratio of $\nu = 0.3$ and a Young's modulus of $E = 1$, except where explicitly stated otherwise. All geometrical dimensions and force magnitudes have been normalized from the International System of Units (SI), thus ensuring coherent correspondence with all non-dimensionalized variables. The penalty parameters were set to $\varrho_{kl}^{LE} = 10^3$ and $\varrho_{kl}^{R} = 10^5$. The degree of the NURBS representing the geometries and the level set wad set to three for all problems.

For each one of the examples elaborated, the number of elements in each patch is chosen such that the corresponding elements in the physical domain have an approximative uniform distribution. To achieve this desired number of elements, h- and p-refinement are executed, yielding a uniformly distributed knot vector, with the exception of the first and last values, which have multiplicity $d_\alpha + 1$ to guarantee

interpolatory control points in the boundaries. As for the local interpolation of the trimming procedure, polynomials degree two were employed.

To numerically determine the properties of the weaker phase, the properties of the stronger phase are scaled by a small positive factor. The Young's modulus of the stronger phase is multiplied by a factor of 10^{-3} while the Poisson's ratio is kept the same. In addition, the condition $\partial\Omega_N = \partial\mathcal{D}_N$ in the set of admissible shapes in (36) is fulfilled by artifially increasing by a factor of 10^3 the stiffness elements of $\mathbf{L}$ corresponding to the zones $\mathcal{D}_N$. Additionally, for the stress-constrained cases, we also consider that the von Mises stress is zero on these regions when computing the shape derivative.

7.1 Example 1: multi-patch non-conforming cantilever 1.6×1

The first problem aims to validate the approach on the classical cantilever beam setting (see Allaire and Jouve (2008), for instance), which we represent in this context as a multi-patch geometry with two non-matching patches. Both are parameterized with a rectangular NURBS thick shell of dimensions 0.8×1.0 and thickness $\epsilon = 0.01$. An in-plane concentrated force of direction $-\mathbf{e}_2$ and magnitude 10^{-4} is applied on the patch $\mathcal{D}_1$ domain at global position position $(1.6, 0.5)$, as illustrated in Figure 10. The patches $\mathcal{D}_0$ and $\mathcal{D}_1$ were discretized with 90×90 and 80×80 elements respectively, resulting in a non-matching interface γ_{10}.

This example is set as a minimization of the volume and the norm L^2 with a fixed parameter $\Lambda^P = 2$. Initially, the optimization was executed without stress constraints, which resulted on a optimal shape with maximum von Mises stress of 0.46. Subsequently, a fictitious material with a yield stress $\sigma_Y = 0.35$ is considered, and the stress constraint of $\sigma_{vm} < \sigma_Y$ is imposed while maintaining the parameter value of $\Lambda^P = 2$. To enforce this condition, a fixed penalization parameter $\Lambda^Q = 10^4$ is applied with in two distinct penalization functions Φ_q given by $q = 4$ and $q = 6$. The resulting stress distributions for the different optimization cases are displayed in Figure 11.

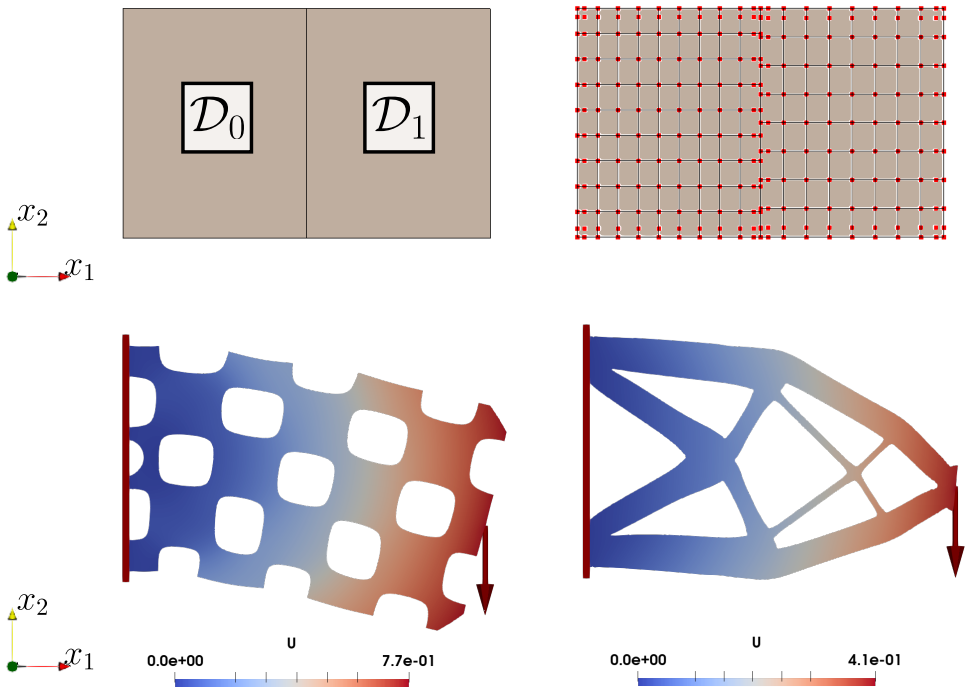

Fig. 10: Example 1 - cantilever beam 1.6×1.0 with one vertical concentrated force. On the top panel, the CAD geometry of the optimization domain along with a coarse proportional representation of the used control points. On the bottom, the deformed configuration is displayed along with the magnitude of the corresponding displacement field. One can also observe the loads and boundary conditions applied to the optimization domain $\mathcal{D}$.

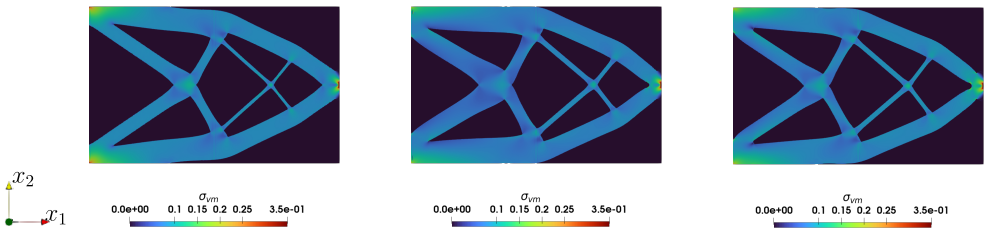

Fig. 11: Example 1 - cantilever beam 1.6×1.0 with one vertical concentrated force. Optimal designs for the cantilever beam in a volume and L^2 norm minimization. From left to right: the von Mises stress distribution for the unconstraint and the constraint cases for $q = 4$ and $q = 6$.

The evolution of the objective function, the volume and the L^2 norm of the von Mises stress are displayed in Figure 12. One can also observe the evolution of the maximum stress computed in the integration points during the trimming procedure, as well as the penalization function Φ_q. The plots indicate that when $q = 4$, the process converges to a suboptimal condition, as evidenced by the value of the maximum stress approaching only 86% of σ_Y. In contrast, when $q = 6$, the volume was reduced until the maximum von Mises stress reached a value corresponding to 96% of the yield stress.

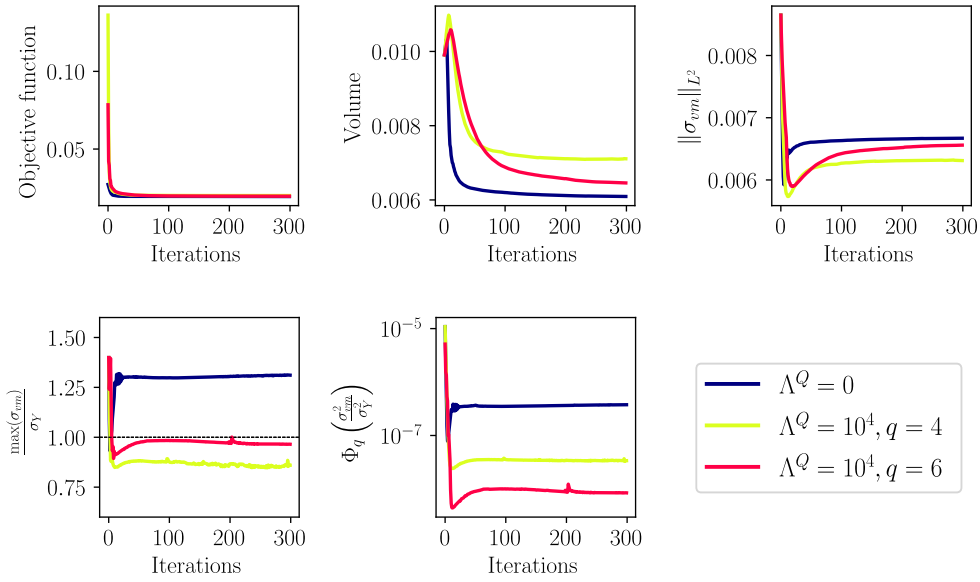

Fig. 12: Example 1 - cantilever beam 1.6×1.0 with one vertical concentrated force. On the top, the evolution of the objective function, the L^2 norm of the von Mises stress and the volume with the increasing number of iterations shows the convergence of the optimization process. On the bottom, the evolution of the maximum von Mises stress computed in the integration points and the penalization function Φ_q.

7.2 Example 2: conforming multi-patch L-shape

The second example under examination is dedicated to validate the approach on structure with stress concentration points, based on a geometry studied in Holmberg et al. (2013). The optimization domain is a L-shaped geometry, represented by two rectangular patches of thickness $\epsilon = 0.01$ and dimensions indicated in Figure 13. For the IGA discretization, the side of unit length in patch $\mathcal{D}_0$ is partitioned into 80 elements, while the others dimensions are discretized to ensure a uniform element size in the physical space, which results in a total of 11289 elements. The optimization problem is set as a unconstraint minimization of the volume and the p-norm considering $p = 6$ and $\Lambda^P = 1.5$. In Figure 13, one can observe that the optimized shape avoids having a sharp corner on the point with stress concentration.

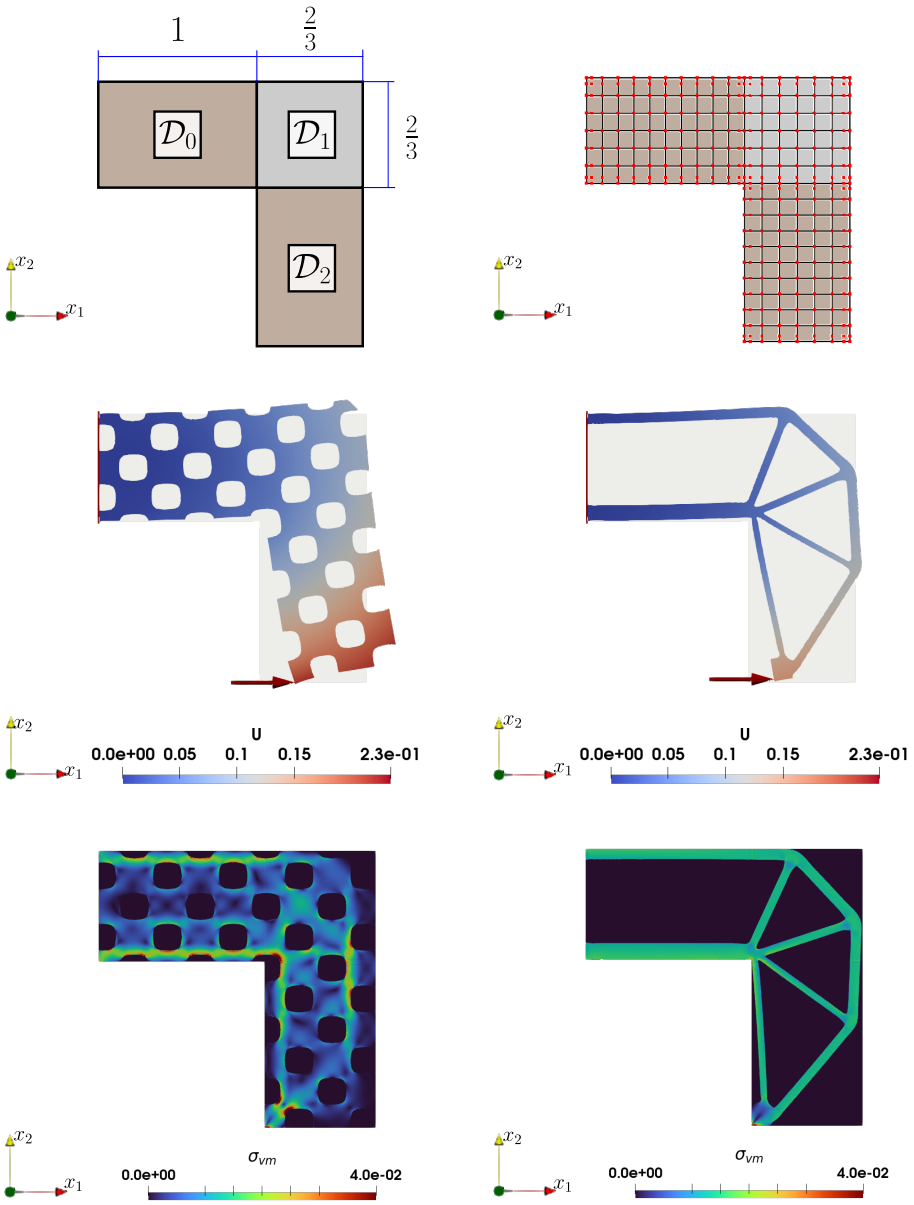

Fig. 13: Example 2 - L shape thick-shell. On the top panel, the CAD geometry of the optimization domain along with a coarse proportional representation of the used control points. On the middle, the deformed configuration is displayed along with the magnitude of the corresponding displacement field. One can also observe the loads and boundary conditions applied to the optimization domain $\mathcal{D}$. On the bottom, the von Mises stress is shown in a non-deformed configuration, where one can also visualize the entire optimization domain. On the left, the shape corresponding to the initialization of the optimization is displayed. On the right, one can see the optimal shape for the norm L^6 obtained on iteration 500.

7.3 Example 3 - non-conforming quarter annulus

The following example explores a multi-patch optimization domain in the form of in-plane arched domain, designed to validate the approach on domains with curved interfaces and non-matching discretizations. We consider two patches composing the quarter annulus, depicted in Figure 14, of internal and external radius of 1 and 2, respectively. For the IGA discretization, the straight sides of the quarter annulus of patches $\mathcal{D}_0$ and $\mathcal{D}_1$ are discretized with 51 and 53 elements, yielding a total of 12692 elements.

Similar to Example 1, we first run the unconstraint optimization for the norm L^2 with a fixed parameter $\Lambda^P = 1.9$. The maximal von Mises stress found in the integration points during this process was 0.42. Next, we perform a second optimization process this time constraining the stress to a value inferior to the maximum stress of the unconstraint optimum, namely $\sigma_Y = 0.35$. The penalization parameter Λ^Q was set to 10^3 and $q = 12$. This process yields the shapes shown on the right of Figure 14, in which the contour of the constrained optimum is illustrated in red over the unconstrained shape.

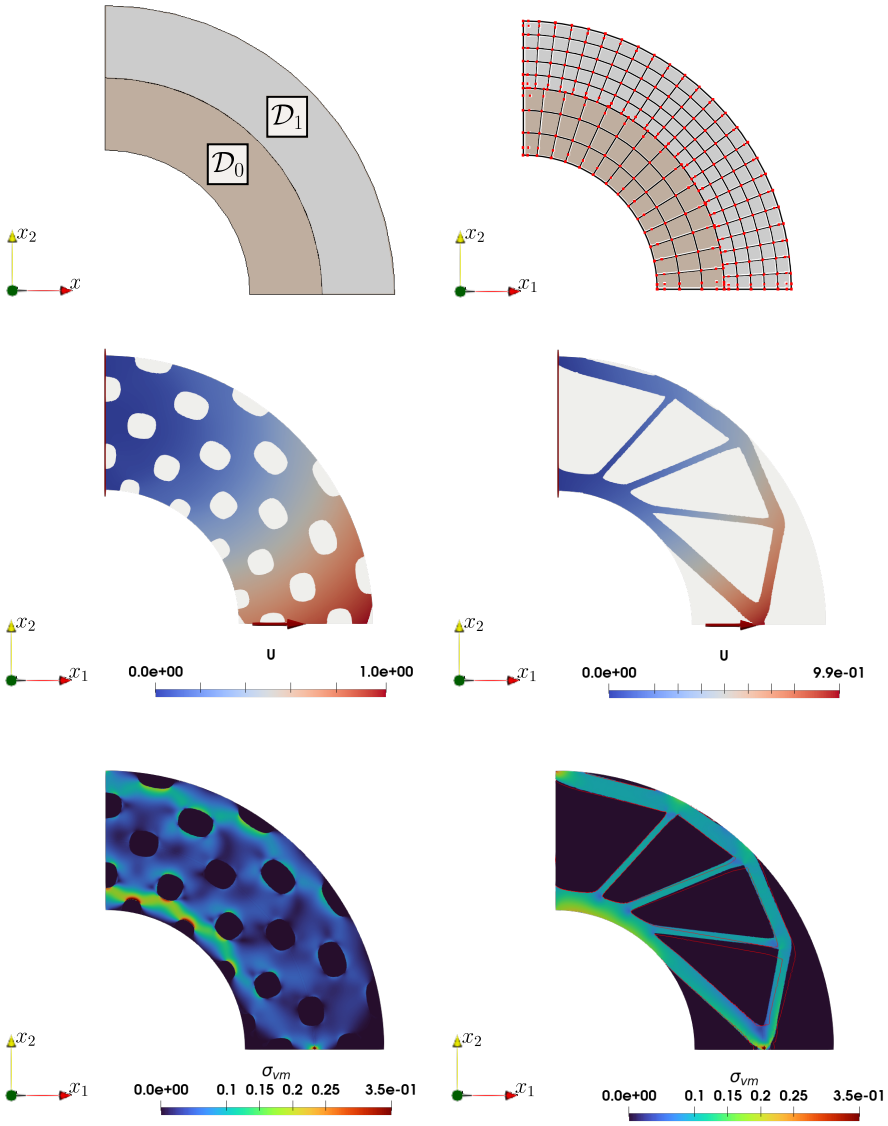

Fig. 14: Example 3 - quarter annulus. On the top panel, the CAD geometry of the optimization domain along with a coarse representation of the used control points. On the middle, the deformed configuration is displayed along with the magnitude of the corresponding displacement field. One can also observe the loads and boundary conditions applied to the optimization domain $\mathcal{D}$. On the bottom, the von Mises stress is shown in a non-deformed configuration, where one can also visualize the entire optimization domain, as well as the contour of the constrained optimal shape. On the left, the shape corresponding to the initialization of the optimization is displayed. On the right, one can see the optimal shape obtained on iteration 145.

The convergence of the objective function, the L^2 norm of the von Mises stress, the volume are displayed in Figure 12. The evolution of the maximum stress in the domain, as well as the penalization function Φ_q are also displayed through the iterations. The constraint optimization converges to a value 2.5% above the yield stress.

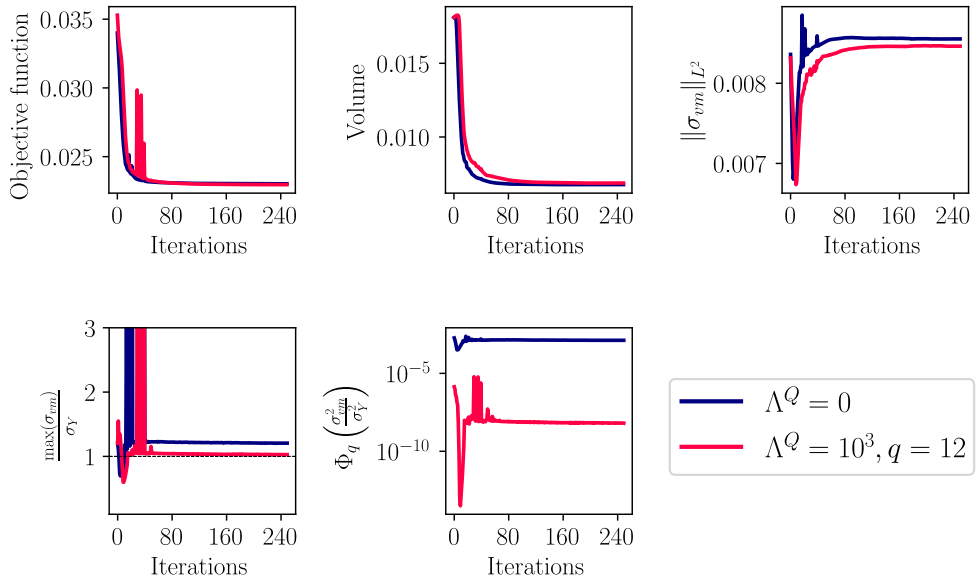

Fig. 15: Example 3 - quarter annulus. On the top, the evolution of the objective function, the L^2 norm of the von Mises stress and the volume with the increasing number of iterations shows the convergence of the optimization process. On the bottom, the evolution of the maximum von Mises stress computed in the integration points and the penalization function Φ_q.

7.4 Example 4: conforming multi-patch T-shape

In the subsequent problem, the method is tested on a geometrially conforming multi-patch T-shape domain under an out-plane load, as depicted in Figure 16, as proposed in Ho-Nguyen-Tan and Kim (2021). This configuration comprises of four identical shells of dimension 20×20, each with a thickness of $\epsilon = 0.5$ and Young modulus $E = 2.1 \cdot 10^5$. At the position indicated in Figure 16, a force of magnitude one is distributed symmetrically on five boundary adjacent control points. The NURBS surfaces are discretized with 60×60 each, resulting in a matching discretization with a total of 14400 elements.

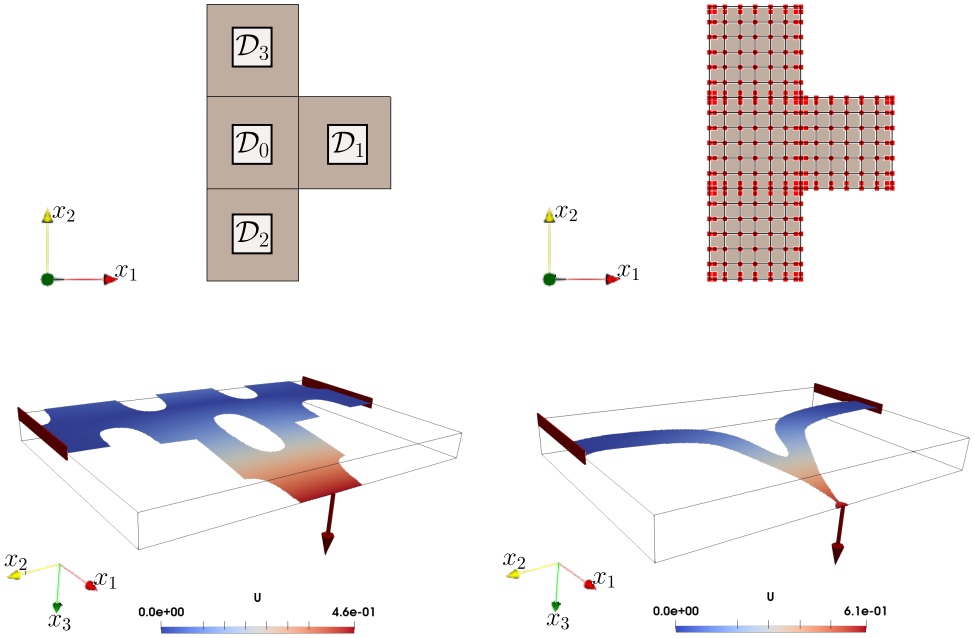

Fig. 16: Example 4 - T-shape. On the top panel, the CAD geometry of the optimization domain along with a coarse proportional representation of the used control points. On the bottom, the deformed configurations of the initialization and optimal shape for $p = 12$ are displayed along with the magnitude of the corresponding displacement field. One can also observe the loads and boundary conditions applied to the optimization domain $\mathcal{D}$.

The objective of this configuration is to demonstrate how an increase in p corresponds to a more accurate approximation of the maximal stress. Two unconstrained optimization problems are solved for minimizing the volume and the p-norm for $p = 2$ and $p = 12$. The values of the parameter Λ^P are respectively set to 4.12 and 5.25. For these parameters values, both processes converge to the same volume fraction of 0.13 within a relative difference $< 0.1\%$, thereby enabling a direct comparison between the shapes. In Figure 17, one can visualize how the optimal shape corresponding to the L^{12} is more effective in avoiding to obtain stress concentration points. The maximum stress of the L^2 optimal shape is 122, which is reduced to 65 when $p = 12$.

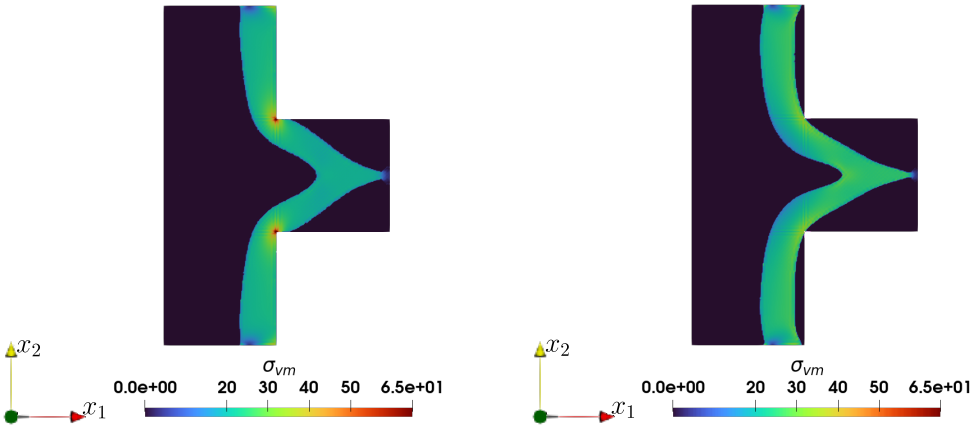

Fig. 17: Example 4 - T-shape. Comparison between optimal shapes obtained for p-norm when $p = 2$ (left) and $p = 12$ (right) for a fixed volume fraction of 0.13. The von Mises stress is shown in a non-deformed configuration, where one can also visualize the entire optimization domain.

7.5 Example 5: conforming cantilever 3D

In the next example, we address a conforming multi-patch domain as depicted in Figure 18. This geometry is defined with eight patches, each with a thickness of $\epsilon = 0.1$, to which two concentrated forces of magnitude 10^{-4} are applied at the indicated position. In the IGA spatial discretization for linear elasticity and regularization, we chose in each patch a parametric discretization such that the elements in the physical domain are uniformly distributed. With this condition, the length L_1 subdivided with uniformity using 100 elements, resulting in a total of 21186 elements. We consider a unconstraint minimization of the volume and L^2 norm with $\Lambda^P = 180$.

This example allows us to obtain a three dimensional representation of the cantilever beam in Example 1. As also pointed out in Allaire and Jouve (2008), the cantilever beam example has an optimal solution similar for compliance and von Mises stress minimization. In Hübner Scherer et al. (2024) we tested this example for the compliance minimization, also obtaining a nearly identical solution to that of the present three dimensional equivalent.

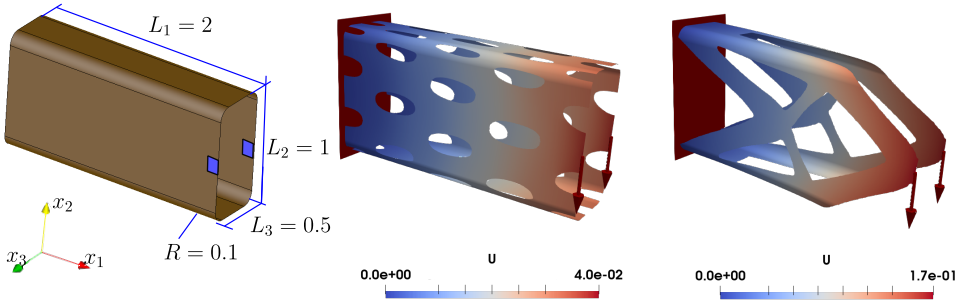

Fig. 18: Example 5 - conforming cantilever 3D. From left to right: the optimization domain, the initial deformed shape with the applied loads and the final optimal deformed solution found after 57 iterations. The blue zones on the left geometry represent the stiffness region for the regularization problem. The colors on both deformed configurations are set using the same scale and correspond to the magnitude of the displacement field.

We present the evolution of the optimization process in Figure 19, where the plots of the objective function, the L^2 norm of the von Mises stress and the volume. Three different stages of the shape's evolution are presented. After 13 iterations, the shape is already quite similar to that obtained at iteration 57, as shown in more detail in Figure 20.

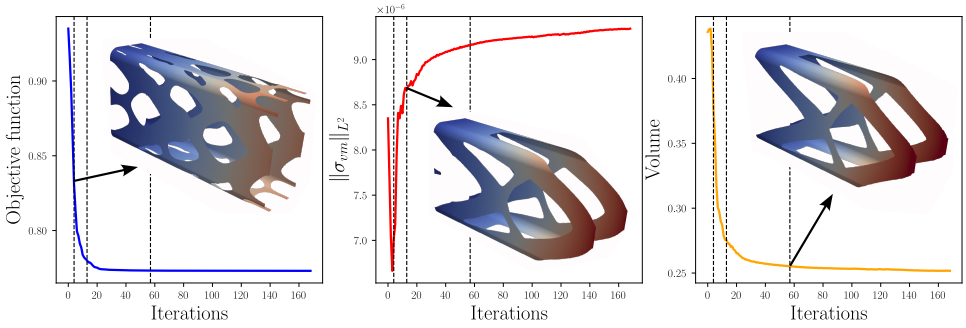

Fig. 19: Example 5 - conforming cantilever 3D. The evolution of the objective function, the norm L^2 and the volume with the increasing number of iterations shows the convergence of the optimization process. The evolution of the shape is displayed at iterations 4, 13 and 57.

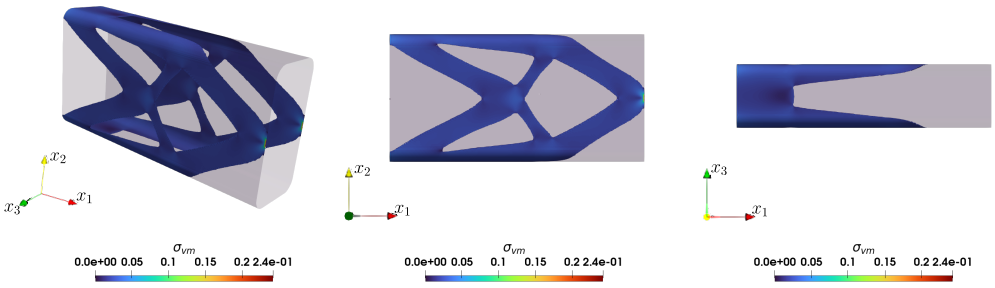

Fig. 20: Example 5 - conforming cantilever 3D. The optimal shape obtained at iteration 57 and its corresponding von Mises stress field.

7.6 Example 6: torsion of a cylinder

The final problem under examination demonstrates the robustness of the approach in predominantly curved geometries. In this example, two concentrated forces of magnitude 10^{-4} create a torsional load applied to a cylindrical structure composed of four patches of thickness $\epsilon = 0.1$, as illustrated in Figure 21. The cylinder was discretized with 80 elements in the $\mathbf{e}_3$ direction. A commensurate refinement was applied in the perpendicular direction so that a uniform element distribution is obtained in the physical domain, yielding a total of 16000 elements. The problem is set as an unconstraint minimization of the volume and the L^2 norm with a fixed multiplier $\Lambda^P = 160$.

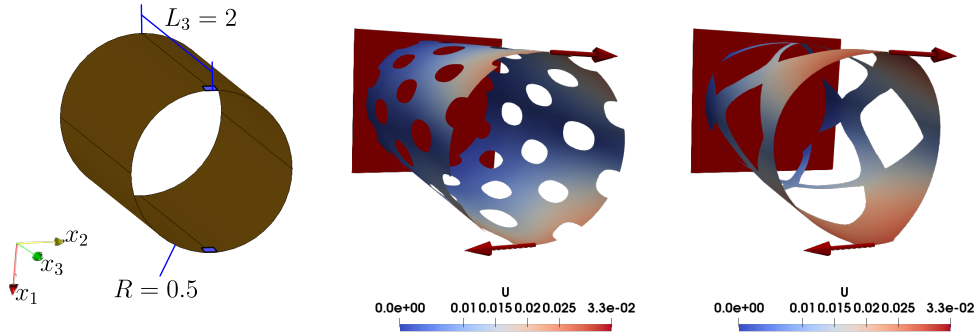

Fig. 21: Example 6 - torsion of a cylinder. From left to right: the optimization domain, the initial deformed shape with the applied loads and the final optimal deformed solution found after 145 iterations. The blue zones on the left geometry represent the stiffness region for the regularization problem. The colors on both deformed configurations are set using the same scale and correspond to the magnitude of the displacement field.

In Figure 22, one can visualize the evolution of the algorithm through the plots of the objective function, the norm L^2 of the von Mises stress and the volume, as they

vary with the increasing number of iterations. This figure highlights three stages of this evolution, observed at iterations 4, 23, and 145.

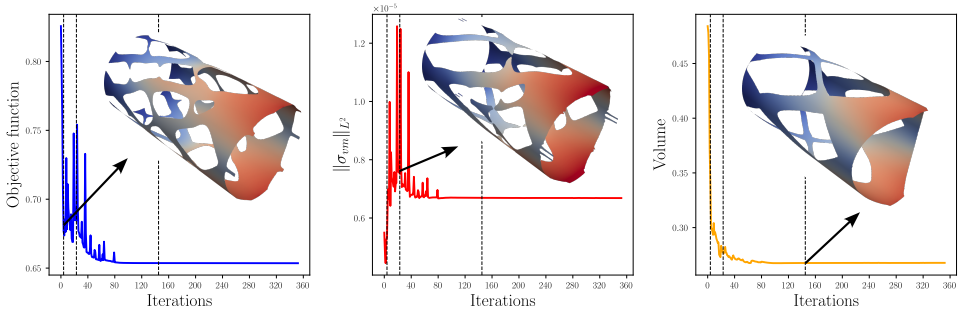

Fig. 22: Example 6 - torsion of a cylinder. The evolution of the objective function, the norm L^2 of the von Mises stress and the volume with the increasing number of iterations shows the convergence of the optimization process. The evolution of the shape is displayed at iterations 4, 23 and 145.

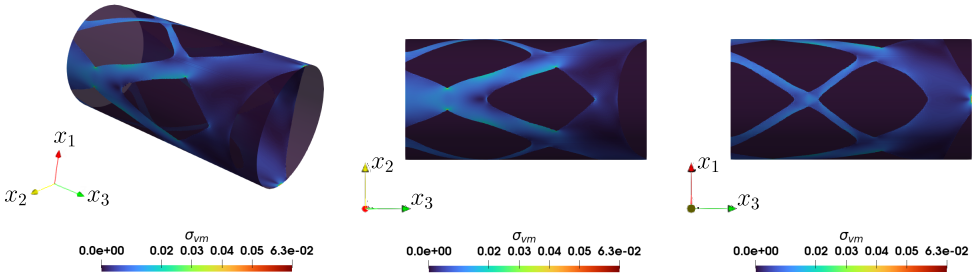

Fig. 23: Example 6 - torsion of a cylinder. The optimal shape obtained at iteration 152 and its corresponding von Mises stress field.

8 Conclusion

We proposed a level set based topology optimization algorithm for non-conforming multi-patch geometries with trimming isogeometric analysis. The numerical results suggests that the presented method allows to find optimal shapes with smooth CAD curves of the domain boundaries, which is well suited for industrial applications and, in particular, additive manufacturing.

We believe that this approach could be easily extended in the future to other relevant objective functions, such as multi-loading conditions Allaire and Jouve (2005), maximizing the smallest eigen-frequency, as showcased in Allaire and Jouve (2005); Xu et al. (2019), and targeting a desired behavior, as in Allaire et al. (2004); Agnelli

et al. (2022). Another interesting possibility is to apply this technique to investigate the effect of randomly distributed quantities, for instance Young's modulus or the shell thickness, on the the optimal shapes, as in Koh and Cirak (2023); Chu et al. (2021); Khristenko et al. (2022).

Acknowledgements. The authors gratefully acknowledge the financial and technical collaboration with STELLANTIS, under ANRT CIFRE contract number 2021THESE0409/01636_22_00019.

Declarations

Conflict of interest. The authors declare that they have no conflict of interest.

Replication of results. In accordance with the proprietary nature of the codes utilized in this research, which are the intellectual property of Stellantis, the company financing the research that yielded the results in this paper, the algorithmic details are not available for public dissemination. For inquiries regarding the methodologies employed or any further information, interested parties are encouraged to directly contact the authors.

References

Amstutz, S., Andrä, H.: A new algorithm for topology optimization using a level-set method. Journal of Computational Physics **216**(2), 573–588 (2006) https://doi.org/10.1016/j.jcp.2005.12.015

Agnelli, F., Constantinescu, A., Nika, G.: Design and testing of 3d-printed micro-architectured polymer materials exhibiting a negative poisson's ratio. Continuum Mechanics and Thermodynamics **32**(2), 433–449 (2020) https://doi.org/10.1007/s00161-019-00851-6

Adam, N.: Méthodes isogéométrique multipatch pour des coques épaisses non linéaires avec contact. Theses, Institut Polytechnique de Paris (September 2020). https://theses.hal.science/tel-02982163

Allaire, G., Jouve, F.: A level-set method for vibration and multiple loads structural optimization. Computer Methods in Applied Mechanics and Engineering **194**(30), 3269–3290 (2005) https://doi.org/10.1016/j.cma.2004.12.018

Allaire, G., Jouve, F.: Minimum stress optimal design with the level set method. Engineering Analysis with Boundary Elements **32**(11), 909–918 (2008) https://doi.org/10.1016/j.enganabound.2007.05.007 . Shape and Topological Sensitivity Analysis: Theory and Applications

Allaire, G., Jouve, F., Toader, A.-M.: Structural optimization using sensitivity analysis and a level-set method. Journal of Computational Physics **194**(1), 363–393 (2004) https://doi.org/10.1016/j.jcp.2003.09.032

Amstutz, S., Novotny, A.A.: Topological optimization of structures subject to von mises stress constraints. Structural and Multidisciplinary Optimization **41**(3), 407–420 (2010) https://doi.org/10.1007/s00158-009-0425-x

Agnelli, F., Nika, G., Constantinescu, A.: Design of thin micro-architectured panels with extension–bending coupling effects using topology optimization. Computer Methods in Applied Mechanics and Engineering **391**, 114496 (2022) https://doi.org/10.1016/j.cma.2021.114496

Adam, N., Tallec, P., Zarroug, M.: Multipatch isogeometric mortar methods for thick shells. Computer Methods in Applied Mechanics and Engineering **372**, 113403 (2020) https://doi.org/10.1016/j.cma.2020.113403

Alacoque, L., Watkins, R.T., Tamijani, A.Y.: Stress-based and robust topology optimization for thermoelastic multi-material periodic microstructures. Computer Methods in Applied Mechanics and Engineering **379**, 113749 (2021) https://doi.org/10.1016/j.cma.2021.113749

Benson, D.J., Bazilevs, Y., Hsu, M.C., Hughes, T.J.R.: Isogeometric shell analysis: The reissner-mindlin shell. Computer Methods in Applied Mechanics and Engineering **199**(5), 276–289 (2010) https://doi.org/10.1016/j.cma.2009.05.011 . Computational Geometry and Analysis

Chu, S., Guilleminot, J., Kelly, C., Abar, B., Gall, K.: Stochastic modeling and identification of material parameters on structures produced by additive manufacturing. Computer Methods in Applied Mechanics and Engineering **387**, 114166 (2021) https://doi.org/10.1016/j.cma.2021.114166

Ciarlet, P.G., Mardare, C.: An Introduction to Shell Theory. In: Differential Geometry: Theory and Applications vol. 9, pp. 94–184. CO-PUBLISHED WITH HIGHER EDUCATION PRESS, ??? (2008). https://doi.org/10.1142/9789812771476_0002 . https://hal.sorbonne-universite.fr/hal-01077558

Costa, G., Montemurro, M., Pailhès, J.: A general hybrid optimization strategy for curve fitting in the non-uniform rational basis spline framework. Journal of Optimization Theory and Applications **176**(1), 225–251 (2018) https://doi.org/10.1007/s10957-017-1192-2

Dierckx, P.: Curve and surface fitting with splines. In: Monographs on Numerical Analysis (1994). https://api.semanticscholar.org/CorpusID:122918752

Goo, S., Wang, S., Hyun, J., Jung, J.: Topology optimization of thin plate structures with bending stress constraints. Computers & Structures **175**, 134–143 (2016) https://doi.org/10.1016/j.compstruc.2016.07.006

Gao, J., Xiao, M., Zhou, M., Gao, L.: Isogeometric topology and shape optimization for composite structures using level-sets and adaptive gauss quadrature. Composite

Structures **285**, 115263 (2022) https://doi.org/10.1016/j.compstruct.2022.115263

Ho-Nguyen-Tan, T., Kim, H.-G.: Level set-based topology optimization for compliance and stress minimization of shell structures using trimmed quadrilateral shell meshes. Computers & Structures **259**, 106695 (2021) https://doi.org/10.1016/j.compstruc.2021.106695

Holmberg, E., Torstenfelt, B., Klarbring, A.: Stress constrained topology optimization. Structural and Multidisciplinary Optimization **48**, 33–47 (2013) https://doi.org/10.1007/s00158-012-0880-7

Hübner Scherer, F., Zarroug, M., Naceur, H., Constantinescu, A.: Topology optimization of curved thick shells using level set method and non-conforming multi-patch isogeometric analysis. Computer Methods in Applied Mechanics and Engineering **430**, 117205 (2024) https://doi.org/10.1016/j.cma.2024.117205

Jahangiry, H.A., Gholhaki, M., Naderpour, H., Tavakkoli, S.M.: Isogeometric level set-based topology optimization for geometrically nonlinear plane stress problems. Computer-Aided Design **151**, 103358 (2022) https://doi.org/10.1016/j.cad.2022.103358

Koh, K.J., Cirak, F.: Stochastic pde representation of random fields for large-scale gaussian process regression and statistical finite element analysis. Computer Methods in Applied Mechanics and Engineering **417**, 116358 (2023) https://doi.org/10.1016/j.cma.2023.116358

Khristenko, U., Constantinescu, A., Le Tallec, P., Wohlmuth, B.: Statistically equivalent surrogate material models: Impact of random imperfections on the elasto-plastic response. Computer Methods in Applied Mechanics and Engineering **402**, 115278 (2022) https://doi.org/10.1016/j.cma.2022.115278

Kim, H.-J., Seo, Y.-D., Youn, S.-K.: Isogeometric analysis for trimmed cad surfaces. Computer Methods in Applied Mechanics and Engineering **198**(37), 2982–2995 (2009) https://doi.org/10.1016/j.cma.2009.05.004

Kang, P., Youn, S.-K.: Isogeometric topology optimization of shell structures using trimmed nurbs surfaces. Finite Elements in Analysis and Design **120**, 18–40 (2016) https://doi.org/10.1016/j.finel.2016.06.003

Laurain, A.: A level set-based structural optimization code using fenics. Structural and Multidisciplinary Optimization **58**(3), 1311–1334 (2018) https://doi.org/10.1007/s00158-018-1950-2

Lam, S.K., Pitrou, A., Seibert, S.: Numba: a llvm-based python jit compiler. In: Proceedings of the Second Workshop on the LLVM Compiler Infrastructure in HPC. LLVM '15. Association for Computing Machinery, New York, NY, USA (2015). https://doi.org/10.1145/2833157.2833162

Laurain, Antoine, Sturm, Kevin: Distributed shape derivative via averaged adjoint method and applications. ESAIM: M2AN **50**(4), 1241–1267 (2016) https://doi.org/10.1051/m2an/2015075

Liu, H., Yang, D., Hao, P., Zhu, X.: Isogeometric analysis based topology optimization design with global stress constraint. Computer Methods in Applied Mechanics and Engineering **342**, 625–652 (2018) https://doi.org/10.1016/j.cma.2018.08.013

Marussig, B., Hughes, T.J.R.: A review of trimming in isogeometric analysis: Challenges, data exchange and simulation aspects. Archives of Computational Methods in Engineering **25**(4), 1059–1127 (2018) https://doi.org/10.1007/s11831-017-9220-9

Montemurro, M., Mas, A., Zerrouq, S.-e.: Topology and anisotropy optimisation of continua using non-uniform rational basis spline entities. Computer Methods in Applied Mechanics and Engineering **420**, 116714 (2024) https://doi.org/10.1016/j.cma.2023.116714

Montemurro, M., Roiné, T.: Strength-based topology optimisation of anisotropic continua in a cad-compatible framework. Advances in Engineering Software **189**, 103591 (2024) https://doi.org/10.1016/j.advengsoft.2023.103591

Nika, G., Constantinescu, A.: Design of multi-layer materials using inverse homogenization and a level set method. Computer Methods in Applied Mechanics and Engineering **346**, 388–409 (2019) https://doi.org/10.1016/j.cma.2018.11.029

Osher, S., Shu, C.-W.: High-order essentially nonoscillatory schemes for hamilton–jacobi equations. SIAM Journal on Numerical Analysis **28**(4), 907–922 (1991) https://doi.org/10.1137/0728049 https://doi.org/10.1137/0728049

Picelli, R., Townsend, S., Brampton, C., Norato, J., Kim, H.A.: Stress-based shape and topology optimization with the level set method. Computer Methods in Applied Mechanics and Engineering **329**, 1–23 (2018) https://doi.org/10.1016/j.cma.2017.09.001

Sevilla, R., Fernández-Méndez, S., Huerta, A.: Nurbs-enhanced finite element method for euler equations. International Journal for Numerical Methods in Fluids **57**(9), 1051–1069 (2008) https://doi.org/10.1002/fld.1711 https://onlinelibrary.wiley.com/doi/pdf/10.1002/fld.1711

Sevilla, R., Fernández-Méndez, S., Huerta, A.: Nurbs-enhanced finite element method (nefem). International Journal for Numerical Methods in Engineering **76**(1), 56–83 (2008) https://doi.org/10.1002/nme.2311 https://onlinelibrary.wiley.com/doi/pdf/10.1002/nme.2311

Schenk, O., Gärtner, K., Fichtner, W., Stricker, A.D.: Pardiso: A high-performance serial and parallel sparse linear solver in semiconductor device simulation.

Future Generation Computer Systems **18**, 69–78 (2000) https://doi.org/10.1016/S0167-739X(00)00076-5

Seo, Y.-D., Kim, H.-J., Youn, S.-K.: Isogeometric topology optimization using trimmed spline surfaces. Computer Methods in Applied Mechanics and Engineering **199**(49), 3270–3296 (2010) https://doi.org/10.1016/j.cma.2010.06.033

Seo, Y.-D., Kim, H.-J., Youn, S.-K.: Shape optimization and its extension to topological design based on isogeometric analysis. International Journal of Solids and Structures **47**(11), 1618–1640 (2010) https://doi.org/10.1016/j.ijsolstr.2010.03.004

T.J.R. Hughes, Y.B. J.A. Cottrell: 2. NURBS as a Pre-Analysis Tool: Geometric Design and Mesh Generation, pp. 19–68. John Wiley & Sons, Ltd, ??? (2009). https://doi.org/10.1002/9780470749081.ch2 . https://onlinelibrary.wiley.com/doi/abs/10.1002/9780470749081.ch2

T. Roiné, M.M., Pailhès, J.: Stress-based topology optimization through non-uniform rational basis spline hyper-surfaces. Mechanics of Advanced Materials and Structures **29**(23), 3387–3407 (2022) https://doi.org/10.1080/15376494.2021.1896822

Tallec, P.L., Sassi, T.: Domain decomposition with nonmatching grids: Augmented lagrangian approach. Mathematics of Computation **64**(212), 1367–1396 (1995) https://doi.org/10.2307/2153360

Wang, M.Y., Li, L.: Shape equilibrium constraint: a strategy for stress-constrained structural topology optimization. Structural and Multidisciplinary Optimization **47**(3), 335–352 (2013) https://doi.org/10.1007/s00158-012-0846-9

Xu, M., Wang, S., Xie, X.: Level set-based isogeometric topology optimization for maximizing fundamental eigenfrequency. Frontiers of Mechanical Engineering **14**(2), 222–234 (2019) https://doi.org/10.1007/s11465-019-0534-1